Intrinsic bioenergetic adaptations compensate for reduced mitochondrial content in HER2-driven mammary tumors

Sara M Frangos[1], Henver S Brunetta[1], Dongdong Wang[2,3], Maria Joy Therese Jabile[2,3], David W L Ma[1], William J Muller[4], Cezar M Khursigara[5], Kelsey H Fisher-Wellman[6], Gregory R Steinberg[2,3,7], Graham P Holloway[1]

[1]Department of Human Health and Nutritional Sciences, University of Guelph, ON, Canada
[2]Centre for Metabolism, Obesity and Diabetes Research, McMaster University, Hamilton, ON, Canada
[3]Division of Endocrinology and Metabolism, Department of Medicine, McMaster University, Hamilton, ON, Canada
[4]Department of Biochemistry, McGill University, Rosalind and Morris Goodman Cancer Research, Montreal, QC, Canada
[5]Department of Molecular and Cellular Biology, University of Guelph, ON, Canada
[6]Department of Cancer Biology, Medical Center Boulevard, Wake Forest University School of Medicine, Winston-Salem, NC, USA
[7]Department of Biochemistry and Biomedical Sciences, McMaster University, Hamilton, ON, Canada
Corresponding authors: Sara M Frangos (sfrangos@uoguelph.ca) and Graham P Holloway (ghollowa@uoguelph.ca)

ABSTRACT

It is now recognized that mitochondria play a crucial role in tumorigenesis, however, it has become clear that tumor metabolism varies significantly between cancer types. The failure of recent clinical trials attempting to directly target tumor respiration with inhibitors of oxidative phosphorylation has highlighted the critical need for additional studies comprehensively assessing mitochondrial bioenergetics. Therefore, we systematically assessed the bulk tumor and mitochondrial metabolic phenotype between murine HER2-driven mammary cancer tumors and paired benign mammary tissue. Transcriptomic and proteomic profiling revealed that HER2-driven mammary tumors are characterized by a downregulation of mitochondrial genes/proteins compared to benign mammary tissue, including a general downregulation of OXPHOS subunits comprising Complexes I-IV. Despite this observation, mitochondrial respiration supported by both carbohydrate-derived substrates (pyruvate) and lipids (palmitoyl-carnitine) was several-fold higher in HER2-driven tumors which persisted regardless of normalization method (i.e. wet weight, total protein content and when corrected for mitochondrial content). This upregulated respiratory capacity could not be explained by OXPHOS uncoupling; however, several subunits/regulators of Complex V function were not downregulated in the tumors, suggesting possible compensatory effects may contribute to high respiratory rates. Furthermore, tumor mitochondria displayed a smaller and more punctate morphology, aligning with a general reduction in mitochondrial fusion and increase in mitochondrial fission markers, which could contribute to improved OXPHOS efficiency. Together, this data highlights that the typical correlation of mitochondrial content and respiratory capacity may not apply to all tumor types and implicates the activation of mitochondrial respiration supporting tumorigenesis in this model.

INTRODUCTION

The field of cancer metabolism has rapidly evolved in the last decade. A specific focus of many researchers has been on understanding the role of mitochondria in tumorigenesis with the goal to potentially target aspects of mitochondrial metabolism to reduce proliferation[1,2]. It was initially hypothesized that a universal characteristic of cancer cells was dysfunctional oxidative phosphorylation (OXPHOS), as proposed by Otto Warburg in the 1920s[3,4]. This theory spurred interest in studying mitochondria in various cancers, highlighting the diverse mitochondrial phenotypes in this context. While instrumental for OXPHOS, mitochondria are now recognized for their multifaceted roles in regulating cellular homeostasis, including supporting macromolecule biosynthesis[5], maintaining redox balance[6] and generating metabolites that regulate gene transcription[7]. Given their pleiotropic effects within the cell, there is a growing recognition that mitochondria play an essential role in cancer initiation, progression, and metastasis[1], and an appreciation that interrogating mitochondrial bioenergetics in diverse cancers may identify novel therapeutic strategies.

Reductions in the content/activity of mitochondrial enzymes within the tricarboxylic acid (TCA) cycle and electron transport chain (ETC) impairs mitochondrial respiratory capacity and coincides with activating transcriptional programs driving tumorigenesis[8–10]. Indeed, inhibition of succinate dehydrogenase (Complex II) in osteosarcoma cells[8], and renal cell carcinoma[9] enhances cancer growth despite OXPHOS inhibition. Furthermore, in colorectal cancer, age-related Complex I deficiency coincides with reduced respiratory capacity but enhanced serine synthesis and subsequent growth rates[10]. Despite this evidence suggesting that disruptions in mitochondrial bioenergetics contribute to tumor progression, several elegant studies using genetic and pharmacological approaches have solidified that a functional ETC is required for cancer cell growth [6,11,12]. Furthermore, the use of whole-genome sequencing specifically interrogating mtDNA phenotypes across several human cancers has revealed that loss of function mutations in mtDNA genes are often under negative selection[13], suggesting the maintenance of mitochondrial function may support tumorigenesis in some cancers and impairments in mitochondrial metabolism are not a ubiquitous finding. However, mitochondrial content represents one dimension of bioenergetic regulation, and may not fully reflect mitochondrial function *in vivo* where substrate delivery/sensitivity and mitochondrial coupling can be altered independently of mitochondrial content[14]. Therefore, a comprehensive assessment of mitochondrial function, particularly in the context of the mitochondrial proteome, is essential to provide deeper insights into the bioenergetic phenotypes observed in different cancers.

Within this framework, there has been considerable interest in investigating mitochondrial bioenergetics and dynamics in breast cancer subtypes due to the limited therapeutic options for triple-negative breast cancer (TNBC) and therapeutic resistance in breast cancers driven by estrogen (ER), progesterone (PR) and human epidermal growth factor (HER2) receptor amplification[15–17]. Indeed, increases in mitochondrial respiration or "OXPHOS reliance" is associated with poor outcomes in treatment naïve TNBC[18], metastatic ER+ tumors[19], and HER2-driven breast cancers[20]. While inhibiting OXPHOS in this context[18,19] (i.e. with Complex I inhibitor IACS-010759) has shown some pre-clinical success, systemic toxicity has prevented the translation of this strategy to the clinic[21]. Furthermore, it is unclear whether increases in mitochondrial respiration arise from increases in mitochondrial content or intrinsic enhancements in mitochondrial function (i.e. coupling efficiency, substrate delivery/sensitivity) - information that is critical to develop successful mitochondrial-targeted therapies with a wider therapeutic window. Thus, in the current study, we comprehensively assessed the bulk tumor and mitochondrial phenotype between murine HER2-driven mammary cancer tumors and benign mammary tissue in the context of the underlying transcriptome and proteome. Respiratory capacity supported by both pyruvate and lipids was enhanced in HER2-driven tumors even when corrected for mitochondrial content, suggesting intrinsic bioenergetic adaptations may exist to maintain OXPHOS during tumorigenesis in this model.

RESULTS

Mammary tumors from MMTV/neu^{ndl}-YD5 mice display canonical HER2 pathway activation

Cell lines are commonly used to study isolated mechanisms driving tumorigenesis, however, they neglect the variety of cell types in the tissue of origin and the influence of the tumor microenvironment, which is a key regulator of cancer growth[23,24]. To this end, we have utilized tumor and benign mammary tissues from MMTV/neu^{ndl}-YD5 transgenic mice[25] to investigate HER2-driven tumor biology **(Fig.1A).** Signaling events linked to HER2 activation rely on the autophosphorylation of the tyrosine kinase domain[25–27] and MMTV/neu^{ndl}-YD5 mice possess an add-back mutation at the Y1226/7 (YD) site, activating downstream signaling events linked to SHC/GRB2 with similar transforming potential as the wild-type protein[27,28] **(Fig.1B)**. While the proximal signaling events linked to HER2 activation in this model have been described[27], to validate our bulk tissue-based model, we assessed the mRNA (transcriptomics) and protein (quantitative label-free proteomics and western blotting) expression of canonical HER2 pathway members (RAS/MAPK and PI3K/AKT/mTOR pathways) that are well-characterized in various HER2-overexpressing mammary cancer cell lines **(Fig. 1B)**[29–31]. *Her2* transcript levels were increased ~175-fold (**Fig.1C**) and transcripts belonging to the Ras/MAPK (*Hras, Mapk1, Mapk3*) and PI3K/AKT/mTOR (*Pik3cg, Pik3c2a, Pik3c2b, Pikrcg, Pik3c3, Akt3*) pathways were also upregulated in the tumors compared to the benign mammary tissue **(Fig.1D)**. At the protein level, HER2 was readily detectable in mammary tumors by quantitative label-free proteomics but undetectable in paired benign tissues **(Fig.1E)** suggesting enhanced HER2 transcription also manifests as an increase in receptor content in the tumors. Downstream of HER2 activation, the total protein content of p38 MAPK, ERK1/2 and eEF2 were significantly increased in tumors compared to benign tissue detected by western blot **(Fig.1F,G)**. When normalized to total protein, p38 MAPK and eEF2 phosphorylation were not higher in tumors due to proportional increases in total protein abundance, while in contrast, phosphorylated ERK1/2 and mTOR were significantly upregulated suggesting both Ras/MAPK and the PI3k/AKT/mTOR pathways were activated in tumors **(Fig.1H, S-Fig.1)**. Overall, these data demonstrate that mammary tumors display classical hallmarks of HER2-driven cancer cell signaling, allowing for the subsequent investigation of HER2-driven tumor biology and metabolism in this model.

Assessment of the HER2-driven mammary tumor transcriptome

To understand the biology and metabolism of HER2-driven mammary tumors, we assessed their transcriptomes using RNA sequencing. Principal component analysis (PCA) using the entire gene expression profile showed distinct separation between groups **(Fig.2A)**. Visualizing all differentially expressed genes (DEGs) using a volcano plot **(Fig.2B)** and the top 3000 DEGs using a heatmap **(Fig.2C)** revealed several differentially upregulated and downregulated genes between groups where genes involved in MAPK- and AKT-linked signaling, ECM remodelling and cellular stress responses *(Etv1, Dusp6, Papln, Ier3*) were among the most upregulated genes in the tumors and genes involved in lipid metabolism (*Dgat2, Lipe, Cd36*) were among the most downregulated. Enrichment analysis of the top 3000 upregulated DEGs **(Fig.2D)** identified pathways characteristic of HER2-driven signaling (e.g. tyrosine kinase signaling, GTPase signaling) and gene ontology (GO) analysis identified processes indicative of active transcription, translation, and protein turnover characteristic of a rapidly proliferating tissue **(Fig.2E)**. Interestingly, enrichment analysis of the top 3000 downregulated genes in the tumors consistently identified that mitochondrial metabolism, and in particular components of the oxidative phosphorylation (OXPHOS) system were downregulated in tumors compared to benign mammary tissue **(Fig.2F,G)**. Altogether, these data further support that this whole tissue model aligns with canonical HER2-driven cell signaling events and highlights that HER2-driven tumors are characterized by reductions in mitochondrial gene expression.

Assessment of HER2-driven mammary tumor proteome

We further validated our transcriptomic findings at the protein level using label-free quantitative proteomics and detected 2589 proteins in the benign mammary tissue and 2448 proteins in the

143 HER2-driven tumors; 1848 of which were found in both groups **(Fig.3A)**. This initial analysis revealed
144 741 and 600 uniquely expressed (i.e. only detected in one tissue) proteins in benign mammary tissue
145 and tumors respectively **(S-Fig.2A)**. Interestingly, OXPHOS and aerobic respiration proteins were
146 identified among the top pathways in benign tissue, but not in tumors **(S-Fig.2B-G)**, further
147 supporting the notion of downregulated mitochondrial content within tumors. Reflecting the PCA for
148 the transcriptomic data, analysis of all overlapping proteins between benign and tumor samples
149 revealed distinct separation **(Fig.3B)**. Of the 1848 proteins found in both the tumors and benign
150 tissue, 420 were significantly different (p-adj. <0.1, **Fig 3A,C,D**). However, the majority of the
151 differentially expressed proteins were downregulated (n=411) in tumors compared to benign
152 mammary tissue. Upregulated proteins (n=9) included those involved in canonical HER2 signaling,
153 protein synthesis and processing, and glycolytic metabolism **(S-Table 1)**. Supporting transcriptomic
154 data, which indicated a reduction in mitochondrial content and OXPHOS, enrichment analysis
155 revealed that 8 of the top 10 downregulated pathways **(Fig. 3E)** and all top 10 downregulated GO **(Fig.**
156 **3F)** were related to mitochondrial biogenesis and/or metabolism, and OXPHOS was identified in the
157 top 10 downregulated KEGG pathways **(Fig.3G)**. Together, these proteomic data support our
158 transcriptomic analysis suggesting HER2-driven tumors are characterized by lower mitochondrial
159 content than benign mammary tissue.

160 **Integrated assessment of the HER2-driven tumor transcriptome and proteome**

161 Considering both transcriptomic and proteomic data suggest that mitochondrial
162 metabolism/OXPHOS are downregulated in mammary tumors, we also analyzed the 144 overlapping
163 downregulated targets between these analyses **(Fig.4A)**. KEGG enrichment analysis of the
164 downregulated targets identified OXPHOS among the top 10 pathways, as well as carbon
165 metabolism, BCAA degradation and fatty acid metabolism which encompass numerous
166 mitochondrial targets **(Fig.4B)**. The top 10 common downregulated pathways **(Fig.4C)** and GO
167 **(Fig.4D)** all pertained to mitochondrial substrate metabolism/catabolism and OXPHOS. Together,
168 transcriptomic and proteomic analyses strongly support that HER2-driven tumors are characterized
169 by downregulated mitochondrial content.

170 **Assessment of the mitochondrial transcriptome and proteome**

171 Our initial transcriptomic and proteomic analyses encompassed all differentially expressed
172 genes/proteins between tissues (including mitochondrial targets) and clearly identified reductions in
173 mitochondrial content in the tumors. This emphasized the robust nature of mitochondrial
174 adaptations in this model, considering mitochondrial proteins (identified using the MitoCarta 3.0
175 database) represented a small fraction of total cellular protein in both tumors and benign mammary
176 tissue **(S-Fig.3)**. By filtering our proteomic dataset using MitoCarta, we identified 125 mitochondrial
177 proteins that were commonly expressed between the tumors and benign mammary tissue **(Fig.5A)**.
178 When visualizing the 125 proteins with a heatmap, the majority of the mitochondrial proteome was
179 downregulated in the tumors compared to the benign mammary tissue **(Fig.5B)**. The summed
180 absolute abundance of all detected mitochondrial proteins in each group was also lower in tumors
181 **(Fig.5C)**, again supporting our transcriptomic and proteomic analyses suggesting a reduction in
182 mitochondrial content exists in the tumors.

183 While mitochondrial biogenesis is a coordinated process simultaneously upregulating
184 several mitochondrial proteins, the total mitochondrial transcriptome/proteome does not
185 necessarily change proportionally with OXPHOS complex and/or TCA cycle/dehydrogenase content,
186 especially in cancerous tissues. Indeed, reductions in the content of specific respiratory complexes
187 seem to be cancer specific, which can have functional repercussions on mitochondrial respiration
188 rates and/or efficiency[10,32]. Within this context, we assessed the gene expression profile of all
189 OXPHOS complex subunits between groups, which revealed relatively ubiquitous reductions in
190 transcript count (transcripts per million) across subunits of Complexes I-IV **(Fig. 5D-H)**. Interestingly,
191 while the majority of Complex V subunits were also downregulated, this complex had the highest

192 proportion of subunits, displaying no differences between groups **(Fig.5D,I)**. The TCA cycle
193 transcriptome also reflected a general downregulation of transcript abundance, apart from alpha-
194 ketoglutarate dehydrogenase (*Ogdhl*) and succinyl-CoA synthetase GDP forming subunit-β (*Suclg2*),
195 which had a higher transcript abundance in some tumor samples **(Fig.5J)**. While we focused on
196 transcriptomic data for this analysis due to lower detection of certain OXPHOS subunits using label-
197 free quantitative proteomics **(S-Fig.4A-E)**, the summed abundance of all OXPHOS subunits detected
198 per complex expressed relative to the underlying mitochondrial proteome **(S-Fig.4F),** and relative to
199 the total proteome **(S-Fig.4G)** displayed a similar pattern. Overall, these data further suggest that the
200 mitochondrial proteome and OXPHOS complexes I-IV are downregulated in HER2-driven tumors
201 compared to benign mammary tissue.

202 **Mitochondrial respiratory capacity is increased in HER2-driven mammary tumors**

203 Considering our transcriptomic and proteomic data strongly suggest HER2-driven mammary tumors
204 display reductions in mitochondrial content, we next assessed whether this would manifest as a
205 reduction in respiratory capacity by measuring mitochondrial respiratory flux rates. In permeabilized
206 tumors and benign mammary tissue, we assessed basal/endogenous respiration and respiration
207 with saturating carbohydrate (pyruvate/malate) and lipid (palmitoyl-carnitine) substrates. For each
208 protocol, several biological replicates (individual tumors) were utilized, spanning a continuum of
209 whole tumor wet weights/volumes **(S-Fig.5A,B)**. Since no strong correlations were found between
210 tumor wet weight or volume and basal or maximal respiration supported by carbohydrate- or lipid-
211 linked substrates **(S-Fig.5C-J)**, all data points were pooled. When normalizing respiration to tissue
212 wet weight **(Fig. 6A)**, tumors displayed significantly higher basal/endogenous respiration and higher
213 respiration with subsequent additions of pyruvate, malate (CI-linked respiration), ADP (State III
214 respiration), glutamate (CI-linked respiration also supported by alpha-ketoglutarate anaplerosis),
215 and succinate (to maximize CII-linked respiration) **(Fig.6B)**. Equally, tumors displayed significantly
216 higher respiration rates supported by lipids (palmitoyl-carnitine, **Fig.6C**), suggesting that HER2-
217 driven tumors are capable of relying on both substrate sources, perhaps to maximize aerobic
218 metabolism. This initial analysis of respiratory rates was normalized to tissue wet weight, which can
219 be influenced by differences in total and mitochondrial protein content in a given tissue volume. To
220 address this, we first normalized respiratory flux rates to total cellular protein **(Fig.6D,E),** which
221 minimizes differences in factors such as tissue density and hydration that are not directly
222 contributing to mitochondrial oxygen consumption. The third normalization method employed was
223 normalizing respiratory flux to a mitochondrial enrichment factor (MEF) (**Fig.6F,G)** which is the ratio
224 of mitochondrial proteins to the underlying total proteome **(S-Fig.3A,B)**. This approach controls for
225 differences in mitochondrial content between tissues to determine whether increases in respiration
226 are due to increases in mitochondrial content or intrinsic changes in mitochondrial function.
227 Interestingly, the fundamental observation of increased respiratory flux rates in tumors compared to
228 benign tissues was conserved independent of the normalization method, suggesting that HER2-
229 driven mammary tumors are characterized by high respiratory flux rates independent of total cellular
230 protein or reduced mitochondrial protein content. While greater intrinsic OXPHOS was observed with
231 all substrates, lipid supported respiration was stimulated to a greater extent in the tumors, resulting
232 in comparable carbohydrate (pyruvate, malate, ADP) and lipid (palmitoyl-carnitine, malate, ADP)
233 supported respiration **(Fig.7A)**. This effect occurred despite many of the genes and proteins involved
234 in lipid metabolism at the plasma membrane and in the cytosol (e.g. *Acsl1, Adipoq, Dgat1/2, Lipe,*
235 *Fabp4, Cd36, Pparg*) and mitochondria (*e.g. Etfa, Etfb, Etfdh, Hadh, Hadhb, Cpt1b, Cpt2*) being
236 downregulated in tumors compared to benign mammary tissue **(Fig.7B-E)**. The intrinsic activation of
237 respiration was not a ubiquitous finding for all processes linked to OXPHOS, as reactive oxygen
238 species (**S-Fig.6A**) emission rates were higher in tumors compared to benign tissue when normalized
239 to wet weight **(S-Fig.6B)**, lower when normalized to total protein **(S-Fig.6C)** and not different when
240 normalized to mitochondrial content **(S-Fig.6D)**.

241

242 **High respiratory flux rates cannot be explained by OXPHOS uncoupling**

243 Typically, respiratory capacity correlates with mitochondrial content in fully differentiated tissues[32].
244 However, given the apparent discrepancy between mitochondrial/OXPHOS protein content and
245 respiratory flux rates in HER2-driven tumors, we investigated alternative explanations for this
246 observation. One possible explanation for the observed enhanced respiratory rates could be due to
247 the uncoupling of OXPHOS from ATP synthesis, especially when ROS emission is not proportional to
248 respiratory flux. To address this possibility, we utilized oligomycin (OMY) to inhibit the F_0 subunit of
249 ATP synthase (Complex V) and examine its inhibitory potency between groups **(Fig.7F)**. While OMY
250 inhibited respiration in benign mammary tissue by ~55%, respiration in tumors was inhibited by ~80%
251 **(Fig.7G)**. Subsequent additions of antimycin A (AMA) to inhibit Complex III and rotenone (ROT) to
252 inhibit Complex I, fully inhibited respiration in both tissues **(Fig.7G)**. Since respiration was inhibited
253 to a greater extent in the tumors in response to OMY, this protocol strongly suggests that HER2-driven
254 tumor mitochondria are highly coupled.

255 **Tumor mitochondria display altered morphology**

256 When assessing the subcellular ultrastructure of HER2-driven mammary tumors using transmission
257 electron microscopy (TEM), we observed smaller, more punctate mitochondria in tumors compared
258 to benign tissue **(Fig.8A)**. To determine whether ultrastructural observations aligned with the
259 expression of genes and proteins involved in mitochondrial turnover, we filtered our transcriptomic
260 and proteomic dataset using MitoCarta, specifically investigating mitochondrial proteins involved in
261 mitochondrial dynamics and mitophagy. This approach revealed the upregulation of several genes
262 and proteins involved in mitochondrial fission and generally a downregulation of genes and proteins
263 involved in mitochondrial fusion (**Fig.8B-F**). Together, these data show clear morphological
264 differences in tumor versus benign tissue mitochondria, which could potentially influence OXPHOS
265 efficiency.

266 **DISCUSSION**

267 The aim of the current study was to investigate the metabolic characteristics of a mouse model of
268 HER2-driven mammary cancer compared to benign mammary tissue. Specifically, we focused on
269 the bioenergetic adaptations that have occurred with HER2-driven tumorigenesis both with respect
270 to mitochondrial function (respiration and ROS) and mitochondrial content (total mitochondrial
271 proteome and OXPHOS complexes). This investigation revealed several findings: 1) HER2-driven
272 mammary tumors display high respiratory rates compared to benign mammary tissue, 2) tumors are
273 capable of oxidizing lipids and pyruvate to a similar extent despite the downregulation of several
274 genes involved in lipid catabolism, and 3) high tumor respiratory rates cannot be explained by higher
275 mitochondrial content. These data highlight that HER2-driven mammary tumors have the capacity
276 to maintain high OXPHOS rates despite lower mitochondrial content, challenging the typical
277 bioenergetic relationship in fully differentiated tissues.

278 **Relationship between mitochondrial content and function in breast cancer**

279 Studies simultaneously assessing mitochondrial content and mitochondrial respiration and the
280 contribution of these factors to breast cancer malignant transformation are scarce. While reductions
281 in ETC subunit content/activity have been described in mitochondria isolated from human mammary
282 carcinoma cultures compared to mammary epithelial cells[33], it has been assumed that a reduction
283 in ETC subunit content would manifest as a reduction in respiratory capacity. However, this is at odds
284 with several reports that classify breast cancer cells as OXPHOS reliant due to increases in
285 mitochondrial respiration correlating with advanced disease[20,34,35]. Indeed, across many cancers it is
286 generally assumed that mitochondrial content and respiratory function increase or decrease
287 concomitantly, however, recent work has challenged this dogma, demonstrating that high rates of
288 respiration normalized to tissue weight can be negated when corrected for mitochondrial mass,[14,36]
289 revealing intrinsic alterations in cancer cell bioenergetics. In the current study, utilizing this same

290 approach to control for differences in mitochondrial content, we found that respiratory capacity
291 supported by pyruvate and lipids in HER2-driven mammary tumors was significantly higher (~2-4
292 fold) compared to benign mammary tissue despite lower mitochondrial enrichment (total
293 mitochondrial proteome) and lower abundance of several respiratory complex subunits, suggesting
294 intrinsic changes in mitochondrial function/efficiency may explain the acquisition of increased
295 mitochondrial respiratory capacity during HER2-driven tumorigenesis. Several mechanisms could
296 enhance respiration in a mitochondrial-content independent manner, including increased coupling
297 of electron transfer to ATP synthesis (coupling efficiency), changes in the delivery of substrates
298 across the mitochondrial membranes, intrinsic changes in the activity of ETC complexes and/or ATP
299 synthase, and alterations in mitochondrial morphology/dynamics.

300 **OXPHOS efficiency: mitochondrial content-independent mechanisms supporting enhanced**
301 **respiration rates**

302 ***Coupling Efficiency:*** Several studies have suggested that a key function of mitochondrial respiration
303 in cancer cells is the regeneration of NAD^+, FAD and ubiquinone to provide the necessary metabolites
304 for biomass production, rather than ATP synthesis[5,6,37]. From a bioenergetic perspective, this could
305 be achieved by inducing uncoupled respiration, which could manifest in an apparent increase in
306 intrinsic mitochondrial respiration, given that measures of respiratory flux quantify oxygen
307 consumption rather than ATP synthesis. However, in the present study the Complex V inhibitor
308 oligomycin inhibited respiration to a greater extent in HER2-driven tumors, suggesting that
309 uncoupling cannot explain the enhanced respiration rates observed, and if anything, tumors are
310 more coupled than benign mammary tissue. This interpretation aligns with work in MCF7 cells where
311 mitochondrial ATP represents the majority of cellular ATP production[38] suggesting the ATP synthetic
312 function of OXPHOS in breast cancer is likely intact. Indeed, enhanced mitochondrial ATP provision
313 and OXPHOS-dependent biomass expansion are not mutually exclusive processes and increased
314 coupled respiration would satisfy both the bioenergetic and biosynthetic requirements of rapid cell
315 proliferation during tumorigenesis.

316 ***Substrate Delivery and Preference:*** Recent work has highlighted the dependency of HER2+ tumor
317 cells on both lipid (long chain fatty acids) and carbohydrate-derived (pyruvate) substrate for optimal
318 proliferative capacity[40]. In addition to pyruvate, HER2-driven tumors may be particularly poised to
319 utilize lipids, given the proximity of cancer cells to adipocytes in the mammary tumor
320 microenvironment[41], which has spurred interest in inhibiting lipid use/fat oxidation as an adjunct
321 therapy in HER2-driven cancer[40]. Indeed, the use of endogenous substrate may be preferred as solid
322 tumors expand and factors such as increased interstitial fluid pressure and extracellular matrix
323 remodelling impact tumor vessel quality[42], possibly limiting exogenous substrate delivery. However,
324 at the transcript and protein level, enzymes involved in mitochondrial lipid uptake (CPT1, CPT2) and
325 pyruvate uptake (MPC) were largely downregulated compared to benign tissue which would limit
326 rather than enhance mitochondrial substrate delivery. Despite this lower abundance of enzymes
327 supporting mitochondrial substrate delivery, mitochondrial respiration supported by pyruvate and
328 lipids were significantly higher in tumors. Considering lipid and carbohydrate oxidation converge
329 within the mitochondrial matrix, both providing acetyl-CoA to the TCA cycle, it is possible that
330 enhanced OXPHOS efficiency lies at a distal site, implicating intrinsic OXPHOS adaptations as a
331 possible explanation for enhanced respiration in HER2-driven tumors.

332 **Intrinsic OXPHOS Adaptations:** Several cancers are characterized by the altered expression of
333 individual ETC subunits and/or ATP synthase which can have functional repercussions on respiratory
334 function[10,14]. In the current study, despite a consistent downregulation of subunits comprising
335 Complexes I-IV in HER2-driven tumors, a subset of Complex V genes were not downregulated
336 (specifically two subunits of the c-ring of F_0 domain (*Atp5g1, Atp5g2*), two subunits of the F6 domain
337 stalk connecting the F_0 and F_1 domains (*Atp5j1, Atp5j2*), and regulatory proteins ATPase inhibitory
338 factor 1 (*Atpif1*) and distal membrane assembly component 2 (*Dmac2l*)). This shift essentially
339 increases the ratio of ATP synthase/ETC and raises the possibility that a maintenance of these

subunits may enhance OXPHOS rates in the face of downregulated CI-IV subunit content since maximal coupled respiration is usually limited by proton flux through ATP synthase. Indeed, despite mtDNA lesions in proton pumping complexes (I, III and IV) being common in many cancers, presumably reducing the content/function of these complexes, ATP synthase mutations are less common, suggesting positive selection may exist to maintain coupled respiration and ATP production[10,43,44]. Thus, while speculative, it is possible that higher respiration rates in HER2-driven tumors may partially reflect maintained ATP synthase content/function. Alternatively, while bioenergetic efficiency is typically related to intrinsic changes in OXPHOS stoichiometry, mitochondrial morphology can indirectly affect efficiency. We observed smaller, punctate mitochondria in HER2-driven mammary tumors when visualized by TEM, generally aligning with reductions in mitochondrial fusion and increases in mitochondrial fission-related targets. While the direct relationship between mitochondrial morphology and bioenergetics remains contentious, evidence suggests smaller mitochondria (due to enhanced fission or reduced fusion) may be associated with enhanced bioenergetics. Smaller mitochondria tend to have a higher surface-area-to-volume ratio which has been correlated with upregulated OXPHOS in the liver[45], and low rates of respiration is associated with the inhibition of mitochondrial fission[46]. Furthermore, rare genetic mitochondrial diseases are often characterized by hyper-fused mitochondria which is associated with OXPHOS limitations[47]. Indeed, morphological differences in breast cancer mitochondria are well described[17,48–50]and targeting mitochondrial dynamics for therapy is an active area of study[51–53], however, there is a clear need to ascertain the relationship between mitochondrial dynamics and bioenergetics in tumorigenesis.

CONCLUSION

We provide evidence that HER2-driven mammary tumors display enhanced respiratory capacity despite lower mitochondrial content. This increased respiratory capacity could not be explained by changes in OXPHOS coupling, however, differences in mitochondrial morphology and the maintained expression of several subunits of ATP synthase suggest HER2-driven mammary tumors may undergo intrinsic adaptations in mitochondrial function during tumorigenesis.

MATERIALS AND METHODS

Animals and Breeding

All rodent experiments were conducted in accordance with institutional guidelines approved by the Animal Care Committee at the University of Guelph (AUP#5071). MMTV/*neu*^{ndl}-YD5 mice on an FVB background were obtained from Dr. William Muller (McGill University) and Dr. David Ma (University of Guelph). Female MMTV/*neu*^{ndl}-YD5 mice were obtained by breeding male heterozygous MMTV/*neu*^{ndl}-YD5 mice with female FVB mice to yield WT or heterozygous transgenics. Mice were group housed in ventilated cages at room temperature (22ºC) and kept on a 12:12 light-dark cycle with *ad libitum* access to a chow diet and water. Starting at 10 weeks, mice were monitored for tumor development on a biweekly basis for ~10 additional weeks. Mice with tumors exceeding 17 mm in length/width or a volume over 5000 m^3 were euthanized before the 20-week time point.

Tumor and Benign Mammary Tissue Collection

Mice were anesthetized using sodium pentobarbital (60 mg/kg body weight) and checked for depth of anaesthesia by leg retraction after tail pinch. Once under the surgical plane, a ventral incision was made up the midline and the skin separated bilaterally from the underlying fascia to allow for the excision of the intact mammary tumors. Depending on the number of tumors present (typically 1-5), tumors were allocated for mitochondrial function (placed fresh in BIOPS preservation buffer), transmission electron microscopy (fixed in 2.5% glutaraldehyde/1% paraformaldehyde) or snap frozen in liquid nitrogen for further analysis (western blotting, transcriptomics, quantitative label-free proteomics) immediately after whole tumor wet weight was recorded. Paired mammary tissue with no visible tumors, furthest from the site of tumor excision (i.e. if tumors localized in cervical region

benign tissue was harvested from inguinal region) were used as an internal comparison, denoted as benign mammary tissue.

RNA Sequencing and Transcriptomic Analyses

Frozen tissues were homogenized and lysed in TRIzol reagent. After centrifuging, the supernatant (aqueous phase) was applied to the RNeasy kit (Qiagen, 74106) for subsequent total RNA extraction and purification in accordance with the manufacturer's protocol. RNA samples were sent to the McMaster Genomics Facility where an RNA quality check, poly A enrichment, library prep and quality check were performed as previously described[54]. These samples were then run in an Illumina Nextseq P2, 2x50bp sequencing run. FastQC and MultiQC were used for quality control of raw data. Salmon's transcript-level quantification[55] and DESeq2[56] was used to detect DEGs with the threshold of adjusted p-value<0.1. PCA analysis was performed by using variance stabilizing transformation (VST) data through DESeq2 using the pcaExplorer package[57] in R (version 4.2.1). Functional enrichment analysis was performed by GO enrichment analysis[58] and Kyoto Encyclopedia of Genes and Genomes (KEGG) mapping using the GOstats, KEGG.db, and Bioconductor packages. Heatmaps and volcano plots were generated with ggplot2 package using all detected genes or genes sorted by an adjusted p-value<0.1 by false discovery rate method. Detailed descriptions for each analysis are included in the figure descriptions.

Western Blotting

Tumor and benign mammary tissues were homogenized in lysis buffer, diluted to equal protein concentration (1 µg/uL), separated by SDS-PAGE, transferred onto PVDF membranes and detected using enhanced chemiluminescence (ChemiGenius2 Bioimaging System, SynGene, Cambridge, UK) as previously described[59,60]. Commercially available primary antibodies were used to detect total and phosphorylated targets (p38 MAPK (CS9212S, 1:1000), ERK1/2 (CS9102S, 1:1000), Akt (CS4691S, 1:1000), mTOR (CS2972S, 1:1000), p70s6k1 (CS9202S, 1:1000), eEf2 (CS2332S, 1:1000), p-p38 MAPK (CS9211S, 1:1000), p-ERK1/2 (CS9101S, 1:1000), p-AKT (CS9271S, 1:1000), p-mTOR (CS2971S, 1:1000), p-p70s6k1 (CS9234S, 1:1000), p-eEF2 (CS2331S, 1:1000). Due to rapid tissue/protein turnover in tumor tissues, Ponceau staining was an inappropriate loading control, however, trends in total protein targets between groups aligned with quantitative label-free proteomic analyses as a secondary method measuring protein content, validating targets detected by western blotting.

Protein Extraction and Purification for LC-MS

A Bradford assay was used to determine the protein concentration in the samples. Twenty-five µg of protein per lysate was resolubilized with denaturation buffer (6M urea/2M thiourea) and concurrently reduced with 10 mM DTT and alkylated with 20 mM iodoacetamide at RT for 60 min. Samples were precipitated by adding 6:1 v/v cold acetone and kept at -80°C for 60 minutes and the pellet was collected after centrifugation at 10,000g for 10 min at 4°C. Samples were resuspended with 50 mM ammonium bicarbonate and MD-grade trypsin (Thermo Fisher Scientific, Cat#90057) was added at a ratio of 1:50 protease to protein. Digestion occurred overnight at 37°C. After digestion, samples were dried by vacuum centrifugation and purified using Pierce C18 Spin columns (Thermo Fisher Scientific, cat#89873).

LC-MS

The Vanquish Neo UHPLC system was coupled with Orbitrap Exploris 240 mass-spectrometer using the Easy-Spray source for nanoLC-MS protein identification. The Vanquish Neo UHPLC system was configured for trap and elute analysis. Peptides were first trapped and washed on a Pepmap Neo C18 trap column (5 micron, 300 micron x5 mm) then separated on EASY-Spray columns 75 µm I.D. × 50 cm with the maximum pressure of 1200 bar. The nanoLC-MS system was controlled with

434 Standard Instrument Integration (SII) for Xcalibur software. All hardware and data acquisition
435 software were from Thermo Fisher Scientific. The mobile phase A and weak wash liquid was water
436 with 0.1% FA, and the mobile phase B and strong wash liquid was 80% acetonitrile with 0.1% FA. The
437 gradient was as follows 4-19% B over 72 minutes, 19-29% B over 28 minutes, 29-45% B over 20
438 minutes and a 14.5 min wash at 100% B with a flow rate of 300 nL/min. The autosampler temperature
439 was 7 °C, and the column temperature was 45 °C. The sample was injected with Fast Loading set to
440 'Enabled' with Pressure Control at 500 bar. The column Fast Equilibration function was set to
441 'Enabled' with Pressure control at 800 bar, and the equilibration factor was set to 3. Vial bottom
442 detection was set to 'Enabled'.

443 **DDA MS Method**

444 The Orbitrap Exploris 240 MS was operated in DDA mode using a full scan with *m/z* range 375–1500,
445 Orbitrap resolution of 60 000, normalized AGC target value 300%, and maximum injection time set
446 to Auto. The intensity threshold for precursor was set to 1×10^4. MS/MS spectra starting from 120
447 *m/z* were acquired in data-dependent acquisition (DDA) mode with a cycle time of 2 s, where the
448 precursors were isolated in a window of 1.6 Da and subsequently fragmented with HCD using a
449 normalized collision energy of 30%. Orbitrap resolution was set to 15 000 for MS2. The normalized
450 AGC target was standard, and the maximum injection time was set to Auto.

451 **Proteomics data analysis**

452 Analysis of the tissue proteome was performed in R (version 4.2.1) and R Studio (version
453 2024.04.2+764). Principal component analysis was performed using the Vegan package. Volcano
454 plots were created using log2 transformed fold change comparing cancer/benign tissue and -log10
455 adjusted p-value. P-values of differentially regulated proteins between each group were corrected
456 with p.adjust (method = "fdr") within each comparison. Depending on the analysis, heatmaps and
457 volcano plots were generated using all detected proteins or proteins sorted by p.adjust <0.1, detailed
458 descriptions for each analysis are included in the figure descriptions. Gene set enrichment was
459 performed with the Kyoto Encyclopedia of genes and genomes (KEGG)[61] and EnrichR[62].

460 **Mitochondrial Respiration**

461 Mitochondrial respiration experiments were performed using the Oroboros Oxygraph-2k systems at
462 37ºC in MiR05 respiration buffer (0.5 mM EGTA, 3 mM $MgCl_2 \cdot H_2O$, 60 mM potassium lactobionate, 10
463 mM KH_2PO_4, 20 mM HEPES, 110 mM sucrose, 20 mM taurine, and 1 g/L fatty acid free BSA; pH 7.1)
464 with constant stirring at room air saturation (starting at 180 µM O_2). Two-5 mg of permeabilized tumor
465 tissue or 15-20 mg of permeabilized (both permeabilized with 20 µg/µL saponin) mammary tissue
466 were used per 2 mL chamber and each protocol was conducted as at least two technical replicates
467 (duplicate) per tumor or benign sample. Prior to the addition of substrates for any protocol,
468 endogenous (basal) respiration was assessed with no substrates added. Complex I and Complex II
469 supported respiration was assessed with the addition of 5 mM pyruvate and 2 mM malate, 5 mM ADP,
470 10 mM glutamate and 10 mM succinate. In a subset of these experiments, subsequent additions of
471 oligomycin (OMY, 1 µM), antimycin A (AMA, 2.5 µM) and rotenone (ROT, 1 µM) were added to assess
472 OXPHOS coupling. Lipid-supported respiration was assessed with 20 µM palmitoyl-carnitine in the
473 presence of 2 mM malate and 5 mM ADP.

474 **Reactive Oxygen Species Emission**

475 Mitochondrial hydrogen peroxide (H_2O_2) emission was determined fluorometrically (Lumina, Thermo
476 Scientific, Waltham, MA) in permeabilized mammary tissue and mammary tumors as previously
477 described[59] with minor modifications. In brief, 2-5 mg of minced tissue was loaded into a cuvette
478 containing Amplex Red (Invitrogen, Waltham, MA, USA), horseradish peroxidase (5U/mL), saponin

(20 µg/µL), superoxide dismutase (40 U/mL) in Buffer Z (105 mM K-MES, 30 mM KCl, 1 mM EGTA, 10 mM K_2HPO_4, 5 mM $MgCl_2$, 5 µM glutamate, 5 µM malate, 0.5% BSA, pH 7.4). Emission rates were assessed at 37ºC in the presence of 10 mM succinate and calculated using a standard curve generated with known concentrations of H_2O_2.

Data Normalization

Mitochondrial respiration rates and H_2O_2 emission were normalized to individual sample wet weight, group total protein content and group mitochondrial content (mitochondrial enrichment factor, MEF). Total protein content was calculated as a group average (n=6/group) based on a Bradford assay and back-calculated total protein in a given wet weight of starting tissue. Data was normalized to mitochondrial protein by calculating the MEF for each group (n=g/group) based on all detected mitochondrial proteins by quantitative label-free proteomics (Mouse MitoCarta 3.0 database) normalized to total protein abundance per sample as previously described by others[32,36].

Transmission Electron Microscopy

Immediately following tissue dissection, tumor and benign mammary tissues were fixed in 2.5% glutaraldehyde/1% paraformaldehyde overnight at 4ºC. The following day, tissues were washed 3x in 100 mM HEPES buffer in preparation for embedding. Tissue was stained with 1% osmium tetroxide for 3h, washed 3x in HEPES buffer and further stained with 1% uranyl acetate for 3h before washing 2x in HEPES buffer and once in ddH2O. Stained tissue was dehydrated with a graded ethanol series followed by infiltration with LR White resin. Blocks were polymerized at 60ºC for 18 hours before ultramicrotomy. Sections were post-stained with uranyl acetate and lead citrate. Sections were allowed to fully dry before imaging on the FEI Tecnai G2 F20 transmission electron microscope operated under normal conditions at 120 kVe.

Statistical Analysis

Statistical analysis and data visualization was performed using Microsoft Excel, GraphPad Prism (version 10.2.3), R (version 4.2.1) and R Studio (version 2024.04.2+764). All data are presented as mean ± SD and data was considered statistically significant if $p<0.05$. For transcriptomic and proteomic analyses, an adjusted p-value of <0.1 was utilized. Details regarding specific statistical analyses are included in the Results section and within each figure legend.

DATA AVAILABILITY

Data is available from corresponding offers upon request.

ACKNOWLEDGEMENTS

This work is funded by a National Sciences and Engineering Research Council (NSERC) grant by GPH (400362). SMF is funded by an NSERC-CGS doctoral scholarship.

FIGURE LEGENDS

Figure 1. Experimental design and canonical HER2 signaling. A) Schematic of mammary tumors from the mammary fat pad of female MMTV-neu^{ndl}-YD5 mice and adjacent normal (benign) mammary tissue, representative images of tumor morphology (tumor capsule, peripheral tumor tissue and necrotic core), tissue processing workflow for transcriptomics, proteomics, western blotting, mitochondrial respiration, ROS emission, and transmission electron microscopy (TEM). **B)** Schematic of classical signaling pathways (Ras/MAPK and PI3K/AKT/mTOR) downstream of HER2 receptor stimulation in the YD5 model. **C)** *Her2* gene expression (transcripts per million, TPM), **D)** Gene expression for canonical HER2 signaling. **E)** Absolute abundance of HER2 protein detected by quantitative label-free proteomics (n.d. = HER2 not detected in benign). **F)** Representative western blots of proteins involved in canonical HER2 signaling. **G,H)** Quantified western blots (% of benign) for **G)** total protein content and **H)** phosphorylated targets normalized to the total protein content of each target. P-values in panels **D** and **E** listed as adjusted p values from transcriptomic (DEG) data (p-adj. <0.1 considered statistically significant). In panels **G,H** data is presented as means ± SD and statistical significance was determined using an unpaired, two tailed Student's t-test (*=p<0.05, n=5-6 per group/protein target). ***Abbrev.*** *AKT - protein kinase B; eEf2 - eukaryotic elongation factor 2; eIF4E – eukaryotic translation initiation factor 4E; ERK – extracellular signal-regulated kinase;*

GRB2 – growth factor receptor-bound protein-2, MEK – mitogen-activated protein kinase kinase; mTORC1/2 – mechanistic target of rapamycin complex 1 and 2; PDK – 3-phosphoinositide-dependent protein kinase-1; PI3K – phosphoinositide 3-kinase; PIP2/3 – phosphatidylinositol 4,5 bisphosphate, PIP3 – phosphatidylinositol 3,4,5-triphosphate; p70S6k1 – ribosomal protein S6 kinase beta-1; RAF – rapidly accelerated fibrosarcoma; RAS – rate sarcoma virus; SHC – Src homolog and collagen homolog; 4EBP1 – eukaryotic translation initiation factor 4E-binding protein 1.

Figure 2. Assessment of HER2-driven mammary tumor and benign mammary tissue transcriptomes. A) PCA of benign mammary tissue and mammary tumors, **B)** Volcano plot showing differentially expressed genes (DEGs) identified between mammary tissue and mammary tumors. **C)** Heatmap of top 3000 DEGs, **D)** Top 10 upregulated pathways (Reactome 2022) and **E)** gene ontologies (GO Biological Process 2023) in tumors compared to benign mammary tissue, **F)** Top 10 downregulated pathways (Reactome 2022) and **G)** gene ontologies (GO Biological Process 2023) in tumors compared to benign mammary tissue. Panels **D,E** assess the top 3000 upregulated DEGs (log2fc>1), panels **F,G** assess the top 3000 downregulated DEGs (log2fc<1). An adjusted p-value of <0.1 was considered statistically significant across all analyses. The Enrichr open access analysis web tool was used to generate panels **D-G** which were sorted by p-value.

Figure 3. Assessment of HER2-driven mammary tumor and benign mammary tissue proteomes. A) Venn diagram showing all detected proteins. Of the 1848 overlapping targets, 420 were significantly different based on a p-adj. <0.1. **B)** PCA of benign mammary samples and mammary tumors, **C)** Volcano plot showing proteins identified between mammary tumors and benign mammary tissue, those in blue (downregulated) or red (upregulated) were significantly different (n=420 proteins, p-adj. <0.1). **D)** Heatmap of 420 differentially expressed proteins in benign and tumor samples. **E)** Top 10 downregulated pathways (Reactome 2022) and **F)** gene ontologies (GO Biological Process, 2023), **G)** KEGG analysis of downregulated proteins. The Enrichr open access analysis web tool was used to generate panels **E,F** which were sorted by p-value.

Figure 4. Overlapping downregulated genes and proteins between HER2-driven mammary tumor transcriptome and proteome. A) Venn diagram showing 144 overlapping downregulated targets between the assessed HER2-driven tumor and benign mammary tissue transcriptomes and proteomes. **B)** KEGG analysis for common downregulated targets. Top 10 downregulated **C)** pathways (Reactome 2022) and **D)** gene ontologies (GO Biological Process 2023). An adjusted p value of <0.1 was utilized for all analyses. The Enrichr open access analysis web tool was used to generate panels **C,D** which were sorted by p-value.

Figure 5. Assessment of the mitochondrial transcriptome and proteome. A) Venn diagram showing mitochondrial proteins detected in the current dataset when cross-referenced with the Mouse MitoCarta 3.0 database. **B)** Heatmap of 125 mitochondrial proteins identified in benign mammary tissue and HER2-driven tumors (n=5/group). **C)** Absolute abundance of all mitochondrial proteins detected in benign and tumor tissues. **D)** Gene expression (detected by transcriptomics; transcripts per million) of all detected OXPHOS subunits separated per respiratory complex, black and white bars represent subunits with no significant differences between groups. **E-J)** Heatmaps of **E)** Complex I, **F)** Complex II, **G)** Complex III, **H)** Complex IV, **I)** Complex V (ATP synthase) and **J)** TCA cycle transcriptomes. All proteomic analyses **(panels A-C)** were conducted on n=5/group. All transcriptomic analyses **(panels D-J)** were conducted on n=6/group. **Panels B,C** were analyzed using an unpaired two tailed Student's t-test (*p<0.05). In **Panel D**, * and coloured (blue and green bars) represent significant differences between benign and tumor samples based on an adjusted p value of <0.1. OXPHOS complex schematics in panel **D** were obtained from the open access RCSB Protein Data Bank *(Complex I = TW1V, Complex II=2A06, Complex III= 3SFD Complex IV=6NMP Complex V = 5FIL). Bars in panel **D** are listed in the following order: Complex I: Ndufa1, Ndufa10, Ndufa11, Ndufa12, Ndufa13, Ndufa2, Ndufa3, Ndufa5, Ndufa6, Ndufa7, Ndufa8, Ndufa9, Ndufab1, Ndufb10, Ndufb11, Ndufb2, Ndufb3, Ndufb4, Ndufb5, Ndufb6, Ndufb7, Ndufb8, Ndufb9, Ndufc1, Ndufc2, Ndufs1, Ndufs2, Ndufs3, Ndufs4, Ndufs5, Ndufs6, Ndufs7, Ndufs8, Ndufv1, Ndufv2, Ndufv3; Complex II: Sdha, Sdhb, Sdhc, Sdhd; Complex III: Cyc1, Uqcr10, Uqcr11, Uqcrb, Uqcrc1, Uqcrc2, Uqcrfs1, Uqcrh, Uqcrq; Complex IV: Cox4i1, Cox4i2, Cox5a, Cox5b, Cox6a1, Cox6b1, Cox6b2, Cox6c, Cox7a1, Cox7a2, Cox7a2l, Cox7b, Cox7c, Cox8a, Cox8b, Ndufa4; Complex V: Atp5a1, Atp5b, Atp5c1, Atp5d, Atp5e, Atp5g1, Atp5g2, Atp5g3, Atp5h, Atp5j, Atp5j2, Atp5k, Atp5l, Atp5md, Atp5mpl, Atp5o, Atp5pb, Atpif1, Dmac2l.*

Figure 6. Assessment of lipid and carbohydrate linked mitochondrial respiration and OXPHOS coupling in benign mammary tissue and HER2-driven mammary tumors. A) Schematic depicting methods of normalization for respiration rates (*per wet weight, total protein, mitochondrial protein/enrichment*). **B)** Complex I and complex II- supported respiration normalized to tissue wet weight, **C)** lipid-supported respiration normalized to tissue wet weight, **D)** Complex I and complex II-supported respiration normalized to total protein content, **E)** lipid-supported respiration normalized to total protein content, **F)** Complex I and complex II-supported respiration normalized to mitochondrial protein (mitochondrial enrichment factor, MEF). **G)** Lipid supported respiration normalized to mitochondrial protein. All individual values represent biological replicates (n=9-22/group depending on the protocol). Data are presented as means ± SD, statistical analyses were conducted using an unpaired, two-tailed Student's t-test (*p<0.05). ***Abbrev:*** *E = Endogenous, PM = pyruvate (5 mM), malate (2 mM), D = ADP (5 mM), G = glutamate (10 mM), S = succinate (10 mM), PC = palmitoyl-carnitine (20 μM), CI+CII = maximal CI+CII-supported respiration (PMDGS).*

Figure 7. Lipid and carbohydrate linked respiration and lipid metabolism transcriptome and proteome. A) Maximal rates of carbohydrate (pyruvate, malate, ADP) and lipid (palmitoyl-carnitine, malate, ADP) supported respiration in tumors

585 and benign mammary tissue. **B)** Gene expression (transcripts per million) of mitochondrial pyruvate carrier and carnitine
586 palmitoyltransferase isoforms mediating mitochondrial pyruvate and long chain fatty acid transport respectively. **C)**
587 Network interaction showing downregulated (unsupervised analysis) gene clustering in the HER2-driven tumor
588 transcriptome, **D)** Heatmap of differentially expressed genes involved in lipid oxidation. **E)** Heatmap of differentially
589 expressed proteins involved in lipid metabolism. **F)** Representative trace of protocol used to assess mitochondrial coupling.
590 Following maximal rates of complex I and II- supported respiration, 1 μM oligomycin (OMY) was added to inhibit Complex V
591 (ATP synthase), followed by 2.5 μM antimycin-A (AMA) and 1 μM rotenone (ROT) to inhibit complexes III and I respectively.
592 **G)** Group data for experiment depicted in **(F)** depicted as relative inhibition from maximal complex I and II supported
593 respiration (PMDGS) in each group. In panels **A, B, F** and **G** data are presented as means ± SD and statistical analyses were
594 conducted using an unpaired, two-tailed Student's t-test (*p<0.05).

595 **Figure 8. Mitochondrial morphology and assessment of mitochondrial fusion, mitochondrial fission and mitophagy**
596 **transcriptomes and proteomes in benign mammary tissue and HER2-driven tumors. A)** Transmission electron
597 microscopy (TEM) images of tumor and benign samples showing punctate (tumor) versus elongated (benign) mitochondria.
598 **B)** Gene expression (detected by transcriptomics; transcripts per million) of fusion, fission and mitophagy related genes
599 separated per process filtered by MitoCarta, coloured bars and * represent genes with an adjusted p value of <0.1. Black
600 and white bars represent genes with no significant differences between groups. **C)** Heatmap of fusion transcriptome, **D)**
601 Heatmap of fusion proteome, **E)** Heatmap of fission transcriptome, **F)** Heatmap of fission proteome, **G)** Heatmap of
602 mitophagy transcriptome, **H)** Heatmap of mitophagy proteome. TEM images are from independent tumor and benign tissue
603 samples. Heatmaps depict all detected proteins (n=5/group) and transcripts (n=6/group).

604 **Supplementary Figure 1. Absolute phosphorylated protein targets downstream of HER2 activation. A)** Quantified
605 western blots for phosphorylated canonical HER2 signaling proteins (n=5-6/group). Phosphorylation sites are indicated
606 for each target. **B)** Representative blot for each phosphorylated target. Data are presented as mean ± SD and analyzed
607 with an unpaired, two tailed Student's t-test (*p<0.05).

608 **Supplementary Figure 2. Unique HER2-driven tumor and benign mammary tissue proteins. A)** Venn diagram depicting
609 741 and 600 unique proteins identified in benign mammary tissue and HER2-driven tumors respectively, **B)** KEGG analysis
610 of all detected unique benign mammary tissue proteins, **C)** Top 10 pathways (Reactome 2022), **D)** Top 10 gene ontologies
611 (GO Biological Process) in benign mammary tissue, **E)** KEGG analysis of unique HER2-driven tumor proteins, **F)** Top 10
612 pathways (Reactome 2022), **G)** Top 10 gene ontologies (GO Biological Process) in HER2-driven tumors. KEGG, pathway and
613 GO analyses were conducted on all mammary and tumor proteins detected by quantitative label-free proteomics. The
614 Enrichr open access analysis web tool was used to generate panels **C,D,F and G** which were sorted by p-value.

615 **Supplementary Figure 3. Mitochondrial enrichment in benign mammary tissue and HER2-driven mammary tumors.**
616 **A)** Total and mitochondrial (Mouse MitoCarta 3.0) absolute protein abundance assessed by quantitative label-free
617 proteomics. **B)** Mitochondrial enrichment factor (MEF) calculated as the ratio of all detected MitoCarta proteins relative to
618 the underlying total proteome per sample (n=5/group). Statistical analysis was conducted using an unpaired two tailed
619 Student's t-test (*p<0.05). In panel **A**, *# denotes significant differences between both total and MitoCarta proteomes
620 between groups.

621 **Supplementary Figure 4. Proteomic analysis of detected OXPHOS subunits.** Heatmaps showing subunits detected for
622 **A)** Complex I, **B)** Complex II, **C)** Complex III, **D)** Complex IV, **E)** Complex V (ATP synthase) using quantified label-free
623 proteomics. **F)** OXPHOS complex I-V absolute abundance as a percentage of the mitochondrial proteome (n=5/group). **G)**
624 OXPHOS complex I-V absolute abundance as a percentage of the total detected proteome (n=5/group). Data in panels **F,G**
625 are presented as means ± SD and analyzed with an unpaired, two tailed Student's t-test (*p<0.05).

626 **Supplementary Figure 5. Correlation of tumor size and volume with maximal carbohydrate and lipid-supported**
627 **respiration rates. A)** Tumor wet weight (whole tumor post excision), **B)** Tumor volume calculated as a modified ellipse (V
628 =1/2(length*width^2)). **C-F)** Endogenous (no substrate, CI+CII protocol), Endogenous (no substrate, lipid protocol), State 3
629 (5 mM pyruvate, 2 mM malate, 5 mM ADP) and maximal lipid-supported (2 mM malate, 5 mM ADP, 20 μM palmitoyl-
630 carnitine) respiration rates correlated with tissue wet weight. **G-J)** Same respiration data as **(C-F)** but correlated with tumor
631 volume. The Pearson correlation coefficient (R) values are listed for each correlation.

632 **Supplementary Figure 6. Reactive oxygen species emission in benign mammary tissue and HER2-driven mammary**
633 **tumors.** A) Schematic depicting major sites of superoxide emission from respiratory complexes I and III. Superoxide
634 dismutase 2 (SOD2) subsequently catalyzes the dismutation of superoxide into hydrogen peroxide (H_2O_2) which can be
635 measured fluorometrically. **B)** H_2O_2 emission per wet tissue weight, **C)** H_2O_2 emission per total protein, **D)** H_2O_2 emission
636 per mitochondrial protein (MEF, mitochondrial enrichment factor). Statistical analyses were conducted using an unpaired,
637 two-tailed Student's t-test (*p<0.05).

638 **Supplementary Table 1.** List of 9 significantly upregulated proteins between tumor and benign samples, sorted in order of
639 fold change from benign (smallest to largest fold change). General pathways or functions are listed per protein based on ID
640 mapping from the Uniprot protein sequence database. Adjusted p-values are listed per target.

641

REFERENCES

1. Vasan, K., Werner, M., and Chandel, N.S. (2020). Mitochondrial Metabolism as a Target for Cancer Therapy. Cell Metab. *32*, 341–352. https://doi.org/10.1016/j.cmet.2020.06.019.

2. DeBerardinis, R.J., and Chandel, N.S. (2020). We need to talk about the Warburg effect. Nat. Metab. *2*, 127–129. https://doi.org/10.1038/s42255-020-0172-2.

3. Warburg, O. (1924). Über den Stoffwechsel der Carcinomzelle. Naturwissenschaften *12*, 1131–1137. https://doi.org/10.1007/BF01504608.

4. Warburg, O. (1956). On respiratory impairment in cancer cells. Science *124*, 269–270.

5. Sullivan, L.B., Gui, D.Y., Hosios, A.M., Bush, L.N., Freinkman, E., and Vander Heiden, M.G. (2015). Supporting Aspartate Biosynthesis Is an Essential Function of Respiration in Proliferating Cells. Cell *162*, 552–563. https://doi.org/10.1016/j.cell.2015.07.017.

6. Martínez-Reyes, I., Cardona, L.R., Kong, H., Vasan, K., McElroy, G.S., Werner, M., Kihshen, H., Reczek, C.R., Weinberg, S.E., Gao, P., et al. (2020). Mitochondrial ubiquinol oxidation is necessary for tumour growth. Nature *585*, 288–292. https://doi.org/10.1038/s41586-020-2475-6.

7. Morris, J.P., Yashinskie, J.J., Koche, R., Chandwani, R., Tian, S., Chen, C.-C., Baslan, T., Marinkovic, Z.S., Sánchez-Rivera, F.J., Leach, S.D., et al. (2019). α-Ketoglutarate links p53 to cell fate during tumour suppression. Nature *573*, 595–599. https://doi.org/10.1038/s41586-019-1577-5.

8. Sciacovelli, M., Guzzo, G., Morello, V., Frezza, C., Zheng, L., Nannini, N., Calabrese, F., Laudiero, G., Esposito, F., Landriscina, M., et al. (2013). The mitochondrial chaperone TRAP1 promotes neoplastic growth by inhibiting succinate dehydrogenase. Cell Metab. *17*, 988–999. https://doi.org/10.1016/j.cmet.2013.04.019.

9. Cardaci, S., Zheng, L., MacKay, G., van den Broek, N.J.F., MacKenzie, E.D., Nixon, C., Stevenson, D., Tumanov, S., Bulusu, V., Kamphorst, J.J., et al. (2015). Pyruvate carboxylation enables growth of SDH-deficient cells by supporting aspartate biosynthesis. Nat. Cell Biol. *17*, 1317–1326. https://doi.org/10.1038/ncb3233.

10. Smith, A.L., Whitehall, J.C., Bradshaw, C., Gay, D., Robertson, F., Blain, A.P., Hudson, G., Pyle, A., Houghton, D., Hunt, M., et al. (2020). Age-associated mitochondrial DNA mutations cause metabolic remodelling that contributes to accelerated intestinal tumorigenesis. Nat. Cancer *1*, 976–989. https://doi.org/10.1038/s43018-020-00112-5.

11. Tan, A.S., Baty, J.W., Dong, L.-F., Bezawork-Geleta, A., Endaya, B., Goodwin, J., Bajzikova, M., Kovarova, J., Peterka, M., Yan, B., et al. (2015). Mitochondrial genome acquisition restores respiratory function and tumorigenic potential of cancer cells without mitochondrial DNA. Cell Metab. *21*, 81–94. https://doi.org/10.1016/j.cmet.2014.12.003.

12. Weinberg, F., Hamanaka, R., Wheaton, W.W., Weinberg, S., Joseph, J., Lopez, M., Kalyanaraman, B., Mutlu, G.M., Budinger, G.R.S., and Chandel, N.S. (2010). Mitochondrial metabolism and ROS generation are essential for Kras-mediated tumorigenicity. Proc. Natl. Acad. Sci. U. S. A. *107*, 8788–8793. https://doi.org/10.1073/pnas.1003428107.

13. Yuan, Y., Ju, Y.S., Kim, Y., Li, J., Wang, Y., Yoon, C.J., Yang, Y., Martincorena, I., Creighton, C.J., Weinstein, J.N., et al. (2020). Comprehensive molecular characterization of mitochondrial

genomes in human cancers. Nat. Genet. *52*, 342–352. https://doi.org/10.1038/s41588-019-0557-x.

14. Nelson, M.A., McLaughlin, K.L., Hagen, J.T., Coalson, H.S., Schmidt, C., Kassai, M., Kew, K.A., McClung, J.M., Neufer, P.D., Brophy, P., et al. (2021). Intrinsic OXPHOS limitations underlie cellular bioenergetics in leukemia. eLife *10*, e63104. https://doi.org/10.7554/eLife.63104.

15. Wang, Z., Zheng, Z., Jia, S., Liu, S., Xiao, X., Chen, G., Liang, W., and Lu, X. (2022). Trastuzumab resistance in HER2-positive breast cancer: Mechanisms, emerging biomarkers and targeting agents. Front. Oncol. *12*.

16. Avagliano, A., Ruocco, M.R., Aliotta, F., Belviso, I., Accurso, A., Masone, S., Montagnani, S., and Arcucci, A. (2019). Mitochondrial Flexibility of Breast Cancers: A Growth Advantage and a Therapeutic Opportunity. Cells *8*, 401. https://doi.org/10.3390/cells8050401.

17. Baek, M.L., Lee, J., Pendleton, K.E., Berner, M.J., Goff, E.B., Tan, L., Martinez, S.A., Mahmud, I., Wang, T., Meyer, M.D., et al. (2023). Mitochondrial structure and function adaptation in residual triple negative breast cancer cells surviving chemotherapy treatment. Oncogene *42*, 1117–1131. https://doi.org/10.1038/s41388-023-02596-8.

18. Evans, K.W., Yuca, E., Scott, S.S., Zhao, M., Paez Arango, N., Cruz Pico, C.X., Saridogan, T., Shariati, M., Class, C.A., Bristow, C.A., et al. (2021). Oxidative Phosphorylation Is a Metabolic Vulnerability in Chemotherapy-Resistant Triple-Negative Breast Cancer. Cancer Res. *81*, 5572–5581. https://doi.org/10.1158/0008-5472.CAN-20-3242.

19. El-Botty, R., Morriset, L., Montaudon, E., Tariq, Z., Schnitzler, A., Bacci, M., Lorito, N., Sourd, L., Huguet, L., Dahmani, A., et al. (2023). Oxidative phosphorylation is a metabolic vulnerability of endocrine therapy and palbociclib resistant metastatic breast cancers. Nat. Commun. *14*, 4221. https://doi.org/10.1038/s41467-023-40022-5.

20. Rohlenova, K., Sachaphibulkij, K., Stursa, J., Bezawork-Geleta, A., Blecha, J., Endaya, B., Werner, L., Cerny, J., Zobalova, R., Goodwin, J., et al. (2017). Selective Disruption of Respiratory Supercomplexes as a New Strategy to Suppress Her2high Breast Cancer. Antioxid. Redox Signal. *26*, 84–103. https://doi.org/10.1089/ars.2016.6677.

21. Yap, T.A., Daver, N., Mahendra, M., Zhang, J., Kamiya-Matsuoka, C., Meric-Bernstam, F., Kantarjian, H.M., Ravandi, F., Collins, M.E., Francesco, M.E.D., et al. (2023). Complex I inhibitor of oxidative phosphorylation in advanced solid tumors and acute myeloid leukemia: phase I trials. Nat. Med. *29*, 115–126. https://doi.org/10.1038/s41591-022-02103-8.

22. Asgari-Karchekani, S., Aryannejad, A., Mousavi, S.A., Shahsavarhaghighi, S., and Tavangar, S.M. (2022). The role of HER2 alterations in clinicopathological and molecular characteristics of breast cancer and HER2-targeted therapies: a comprehensive review. Med. Oncol. *39*, 210. https://doi.org/10.1007/s12032-022-01817-6.

23. Mun, S., Lee, H.J., and Kim, P. (2024). Rebuilding the microenvironment of primary tumors in humans: a focus on stroma. Exp. Mol. Med. *56*, 527–548. https://doi.org/10.1038/s12276-024-01191-5.

24. de Visser, K.E., and Joyce, J.A. (2023). The evolving tumor microenvironment: From cancer initiation to metastatic outgrowth. Cancer Cell *41*, 374–403. https://doi.org/10.1016/j.ccell.2023.02.016.

25. Ursini-Siegel, J., Schade, B., Cardiff, R.D., and Muller, W.J. (2007). Insights from transgenic mouse models of ERBB2-induced breast cancer. Nat. Rev. Cancer *7*, 389–397. https://doi.org/10.1038/nrc2127.

26. Iqbal, N., and Iqbal, N. (2014). Human Epidermal Growth Factor Receptor 2 (HER2) in Cancers: Overexpression and Therapeutic Implications. Mol. Biol. Int. *2014*, 1–9. https://doi.org/10.1155/2014/852748.

27. Dankort, D.L., Wang, Z., Blackmore, V., Moran, M.F., and Muller, W.J. (1997). Distinct Tyrosine Autophosphorylation Sites Negatively and Positively Modulate Neu-Mediated Transformation. Mol. Cell. Biol. *17*, 5410–5425. https://doi.org/10.1128/MCB.17.9.5410.

28. Dankort, D., Jeyabalan, N., Jones, N., Dumont, D.J., and Muller, W.J. (2001). Multiple ErbB-2/Neu Phosphorylation Sites Mediate Transformation through Distinct Effector Proteins. J. Biol. Chem. *276*, 38921–38928. https://doi.org/10.1074/jbc.M106239200.

29. Ruiz-Saenz, A., Dreyer, C., Campbell, M.R., Steri, V., Gulizia, N., and Moasser, M.M. (2018). HER2 amplification in tumors activates PI3K/Akt signaling independent of HER3. Cancer Res. *78*, 3645–3658. https://doi.org/10.1158/0008-5472.CAN-18-0430.

30. Kirouac, D.C., Du, J., Lahdenranta, J., Onsum, M.D., Nielsen, U.B., Schoeberl, B., and McDonagh, C.F. (2016). HER2+ Cancer Cell Dependence on PI3K vs. MAPK Signaling Axes Is Determined by Expression of EGFR, ERBB3 and CDKN1B. PLoS Comput. Biol. *12*, e1004827. https://doi.org/10.1371/journal.pcbi.1004827.

31. Serra, V., Scaltriti, M., Prudkin, L., Eichhorn, P.J.A., Ibrahim, Y.H., Chandarlapaty, S., Markman, B., Rodriguez, O., Guzman, M., Rodriguez, S., et al. (2011). PI3K inhibition results in enhanced HER signaling and acquired ERK dependency in HER2-overexpressing breast cancer. Oncogene *30*, 2547–2557. https://doi.org/10.1038/onc.2010.626.

32. Boykov, I.N., Montgomery, M.M., Hagen, J.T., Aruleba, R.T., McLaughlin, K.L., Coalson, H.S., Nelson, M.A., Pereyra, A.S., Ellis, J.M., Zeczycki, T.N., et al. (2023). Pan-tissue mitochondrial phenotyping reveals lower OXPHOS expression and function across cancer types. Sci. Rep. *13*, 16742. https://doi.org/10.1038/s41598-023-43963-5.

33. Putignani, L., Raffa, S., Pescosolido, R., Aimati, L., Signore, F., Torrisi, M.R., and Grammatico, P. (2008). Alteration of expression levels of the oxidative phosphorylation system (OXPHOS) in breast cancer cell mitochondria. Breast Cancer Res. Treat. *110*, 439–452. https://doi.org/10.1007/s10549-007-9738-x.

34. Hu, Y., Xu, W., Zeng, H., He, Z., Lu, X., Zuo, D., Qin, G., and Chen, W. (2020). OXPHOS-dependent metabolic reprogramming prompts metastatic potential of breast cancer cells under osteogenic differentiation. Br. J. Cancer *123*, 1644–1655. https://doi.org/10.1038/s41416-020-01040-y.

35. Pacheco-Velázquez, S.C., Robledo-Cadena, D.X., Hernández-Reséndiz, I., Gallardo-Pérez, J.C., Moreno-Sánchez, R., and Rodríguez-Enríquez, S. (2018). Energy Metabolism Drugs Block Triple Negative Breast Metastatic Cancer Cell Phenotype. Mol. Pharm. *15*, 2151–2164. https://doi.org/10.1021/acs.molpharmaceut.8b00015.

36. McLaughlin, K.L., Hagen, J.T., Coalson, H.S., Nelson, M.A.M., Kew, K.A., Wooten, A.R., and Fisher-Wellman, K.H. (2020). Novel approach to quantify mitochondrial content and intrinsic

765 bioenergetic efficiency across organs. Sci. Rep. *10*, 17599. https://doi.org/10.1038/s41598-020-
766 74718-1.

767 37. Luengo, A., Li, Z., Gui, D.Y., Sullivan, L.B., Zagorulya, M., Do, B.T., Ferreira, R., Naamati, A., Ali,
768 A., Lewis, C.A., et al. (2021). Increased demand for NAD+ relative to ATP drives aerobic
769 glycolysis. Mol. Cell *81*, 691-707.e6. https://doi.org/10.1016/j.molcel.2020.12.012.

770 38. Giddings, E.L., Champagne, D.P., Wu, M.-H., Laffin, J.M., Thornton, T.M., Valenca-Pereira, F.,
771 Culp-Hill, R., Fortner, K.A., Romero, N., East, J., et al. (2021). Mitochondrial ATP fuels ABC
772 transporter-mediated drug efflux in cancer chemoresistance. Nat. Commun. *12*, 2804.
773 https://doi.org/10.1038/s41467-021-23071-6.

774 39. Farge, T., Saland, E., de Toni, F., Aroua, N., Hosseini, M., Perry, R., Bosc, C., Sugita, M., Stuani,
775 L., Fraisse, M., et al. (2017). Chemotherapy-Resistant Human Acute Myeloid Leukemia Cells
776 Are Not Enriched for Leukemic Stem Cells but Require Oxidative Metabolism. Cancer Discov. *7*,
777 716–735. https://doi.org/10.1158/2159-8290.CD-16-0441.

778 40. Nandi, I., Ji, L., Smith, H.W., Avizonis, D., Papavasiliou, V., Lavoie, C., Pacis, A., Attalla, S.,
779 Sanguin-Gendreau, V., and Muller, W.J. (2024). Targeting fatty acid oxidation enhances response
780 to HER2-targeted therapy. Nat. Commun. *15*, 6587. https://doi.org/10.1038/s41467-024-50998-
781 3.

782 41. Wang, Y.Y., Attané, C., Milhas, D., Dirat, B., Dauvillier, S., Guerard, A., Gilhodes, J., Lazar, I., Alet,
783 N., Laurent, V., et al. Mammary adipocytes stimulate breast cancer invasion through metabolic
784 remodeling of tumor cells. JCI Insight *2*, e87489. https://doi.org/10.1172/jci.insight.87489.

785 42. Matuszewska, K., Pereira, M., Petrik, D., Lawler, J., and Petrik, J. (2021). Normalizing Tumor
786 Vasculature to Reduce Hypoxia, Enhance Perfusion, and Optimize Therapy Uptake. Cancers *13*,
787 4444. https://doi.org/10.3390/cancers13174444.

788 43. Wu, S., Akhtari, M., and Alachkar, H. (2018). Characterization of Mutations in the Mitochondrial
789 Encoded Electron Transport Chain Complexes in Acute Myeloid Leukemia. Sci. Rep. *8*, 13301.
790 https://doi.org/10.1038/s41598-018-31489-0.

791 44. Schöpf, B., Weissensteiner, H., Schäfer, G., Fazzini, F., Charoentong, P., Naschberger, A., Rupp,
792 B., Fendt, L., Bukur, V., Giese, I., et al. (2020). OXPHOS remodeling in high-grade prostate
793 cancer involves mtDNA mutations and increased succinate oxidation. Nat. Commun. 2020 111
794 *11*, 1–16. https://doi.org/10.1038/s41467-020-15237-5.

795 45. Zhou, Y., Long, D., Zhao, Y., Li, S., Liang, Y., Wan, L., Zhang, J., Xue, F., and Feng, L. (2022).
796 Oxidative stress-mediated mitochondrial fission promotes hepatic stellate cell activation via
797 stimulating oxidative phosphorylation. Cell Death Dis. *13*, 1–15.
798 https://doi.org/10.1038/s41419-022-05088-x.

799 46. Lhuissier, C., Desquiret-Dumas, V., Girona, A., Alban, J., Faure, J., Cassereau, J., Codron, P.,
800 Lenaers, G., Baris, O.R., Gueguen, N., et al. (2024). Mitochondrial F0F1-ATP synthase governs
801 the induction of mitochondrial fission. iScience *27*. https://doi.org/10.1016/j.isci.2024.109808.

802 47. Zou, W., Chen, Q., Slone, J., Yang, L., Lou, X., Diao, J., and Huang, T. (2021). Nanoscopic
803 quantification of sub-mitochondrial morphology, mitophagy and mitochondrial dynamics in
804 living cells derived from patients with mitochondrial diseases. J. Nanobiotechnology *19*, 136.
805 https://doi.org/10.1186/s12951-021-00882-9.

806 48. Ren, K., Zhou, D., Wang, M., Li, E., Hou, C., Su, Y., Zou, Q., Zhou, P., and Liu, X. (2021). RACGAP1
807 modulates ECT2-Dependent mitochondrial quality control to drive breast cancer metastasis.
808 Exp. Cell Res. *400*, 112493. https://doi.org/10.1016/j.yexcr.2021.112493.

809 49. Zhao, J., Zhang, J., Yu, M., Xie, Y., Huang, Y., Wolff, D.W., Abel, P.W., and Tu, Y. (2013).
810 Mitochondrial dynamics regulates migration and invasion of breast cancer cells. Oncogene *32*,
811 4814–4824. https://doi.org/10.1038/onc.2012.494.

812 50. Han, X.-J., Yang, Z.-J., Jiang, L.-P., Wei, Y.-F., Liao, M.-F., Qian, Y., Li, Y., Huang, X., Wang, J.-B.,
813 Xin, H.-B., et al. (2015). Mitochondrial dynamics regulates hypoxia-induced migration and
814 antineoplastic activity of cisplatin in breast cancer cells. Int. J. Oncol. *46*, 691–700.
815 https://doi.org/10.3892/ijo.2014.2781.

816 51. Zamberlan, M., Boeckx, A., Muller, F., Vinelli, F., Ek, O., Vianello, C., Coart, E., Shibata, K.,
817 Christian, A., Grespi, F., et al. (2022). Inhibition of the mitochondrial protein Opa1 curtails
818 breast cancer growth. J. Exp. Clin. Cancer Res. CR *41*, 95. https://doi.org/10.1186/s13046-022-
819 02304-6.

820 52. Yin, M., Lu, Q., Liu, X., Wang, T., Liu, Y., and Chen, L. (2016). Silencing Drp1 inhibits glioma cells
821 proliferation and invasion by RHOA/ ROCK1 pathway. Biochem. Biophys. Res. Commun. *478*,
822 663–668. https://doi.org/10.1016/j.bbrc.2016.08.003.

823 53. Tang, Q., Liu, W., Zhang, Q., Huang, J., Hu, C., Liu, Y., Wang, Q., Zhou, M., Lai, W., Sheng, F., et
824 al. (2018). Dynamin-related protein 1-mediated mitochondrial fission contributes to IR-783-
825 induced apoptosis in human breast cancer cells. J. Cell. Mol. Med. *22*, 4474–4485.
826 https://doi.org/10.1111/jcmm.13749.

827 54. Wang, D., Townsend, L.K., DesOrmeaux, G.J., Frangos, S.M., Batchuluun, B., Dumont, L., Kuhre,
828 R.E., Ahmadi, E., Hu, S., Rebalka, I.A., et al. (2023). GDF15 promotes weight loss by enhancing
829 energy expenditure in muscle. Nature *619*, 143–150. https://doi.org/10.1038/s41586-023-
830 06249-4.

831 55. Patro, R., Duggal, G., Love, M.I., Irizarry, R.A., and Kingsford, C. (2017). Salmon provides fast
832 and bias-aware quantification of transcript expression. Nat. Methods *14*, 417–419.
833 https://doi.org/10.1038/nmeth.4197.

834 56. Love, M.I., Huber, W., and Anders, S. (2014). Moderated estimation of fold change and
835 dispersion for RNA-seq data with DESeq2. Genome Biol. *15*, 550.
836 https://doi.org/10.1186/s13059-014-0550-8.

837 57. Marini, F., and Binder, H. (2019). pcaExplorer: an R/Bioconductor package for interacting with
838 RNA-seq principal components. BMC Bioinformatics *20*, 331. https://doi.org/10.1186/s12859-
839 019-2879-1.

840 58. Mi, H., Muruganujan, A., Huang, X., Ebert, D., Mills, C., Guo, X., and Thomas, P.D. (2019).
841 Protocol Update for large-scale genome and gene function analysis with the PANTHER
842 classification system (v.14.0). Nat. Protoc. *14*, 703–721. https://doi.org/10.1038/s41596-019-
843 0128-8.

844 59. Paglialunga, S., Ludzki, A., Root-McCaig, J., and Holloway, G.P. (2015). In adipose tissue,
845 increased mitochondrial emission of reactive oxygen species is important for short-term high-
846 fat diet-induced insulin resistance in mice. Diabetologia *58*, 1071–1080.
847 https://doi.org/10.1007/s00125-015-3531-x.

60. Miotto, P.M., and Holloway, G.P. (2019). Exercise-induced reductions in mitochondrial ADP sensitivity contribute to the induction of gene expression and mitochondrial biogenesis through enhanced mitochondrial H2O2 emission. Mitochondrion *46*, 116–122. https://doi.org/10.1016/j.mito.2018.03.003.

61. Kanehisa, M., Sato, Y., Kawashima, M., Furumichi, M., and Tanabe, M. (2016). KEGG as a reference resource for gene and protein annotation. Nucleic Acids Res. *44*, D457–D462. https://doi.org/10.1093/nar/gkv1070.

62. Xie, Z., Bailey, A., Kuleshov, M.V., Clarke, D.J.B., Evangelista, J.E., Jenkins, S.L., Lachmann, A., Wojciechowicz, M.L., Kropiwnicki, E., Jagodnik, K.M., et al. (2021). Gene Set Knowledge Discovery with Enrichr. Curr. Protoc. *1*, e90. https://doi.org/10.1002/cpz1.90.

Figure 1

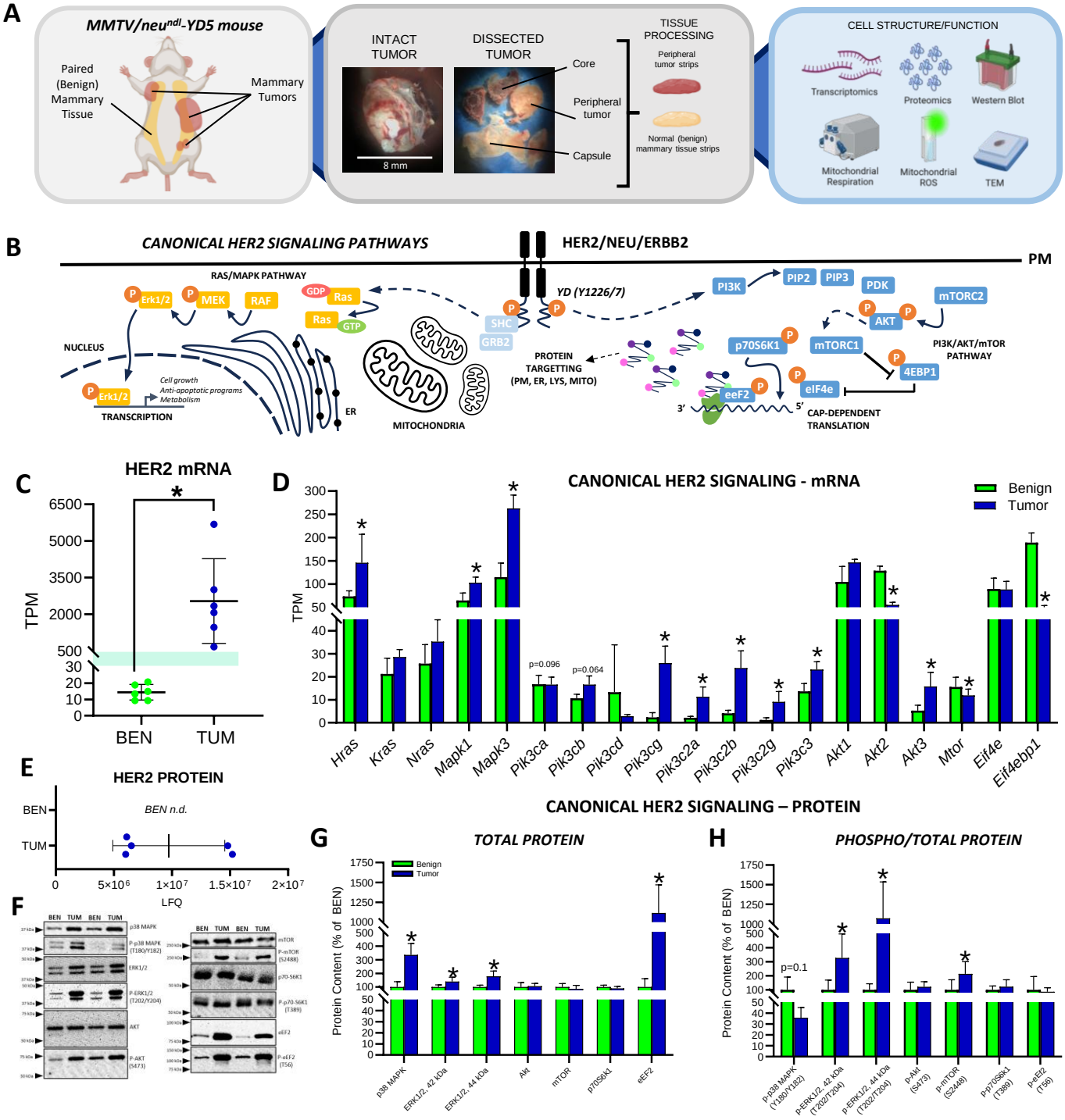
A
MMTV/neu^ndl-YD5 mouse
Paired (Benign) Mammary Tissue
Mammary Tumors
INTACT TUMOR
DISSECTED TUMOR
8 mm
Core
Peripheral tumor
Capsule
TISSUE PROCESSING
Peripheral tumor strips
Normal (benign) mammary tissue strips
CELL STRUCTURE/FUNCTION
Transcriptomics
Proteomics
Western Blot
Mitochondrial Respiration
Mitochondrial ROS
TEM
B
CANONICAL HER2 SIGNALING PATHWAYS
HER2/NEU/ERBB2
PM
RAS/MAPK PATHWAY
Erk1/2
MEK
RAF
GDP
Ras
GTP
NUCLEUS
Cell growth
Anti-apoptotic programs
Metabolism
TRANSCRIPTION
ER
MITOCHONDRIA
YD (Y1226/7)
SHC
GRB2
PROTEIN TARGETTING (PM, ER, LYS, MITO)
PI3K
PIP2
PIP3
PDK
mTORC2
AKT
p70S6K1
mTORC1
4EBP1
eIF4e
eeF2
3'
5'
CAP-DEPENDENT TRANSLATION
PI3K/AKT/mTOR PATHWAY
C
HER2 mRNA
TPM
BEN
TUM
D
CANONICAL HER2 SIGNALING - mRNA
Benign
Tumor
TPM
p=0.096
p=0.064
Hras
Kras
Nras
Mapk1
Mapk3
Pik3ca
Pik3cb
Pik3cd
Pik3cg
Pik3c2a
Pik3c2b
Pik3c2g
Pik3c3
Akt1
Akt2
Akt3
Mtor
Eif4e
Eif4ebp1
E
HER2 PROTEIN
BEN
TUM
BEN n.d.
LFQ
F
BEN TUM BEN TUM
p38 MAPK
P-p38 MAPK (T180/Y182)
ERK1/2
P-ERK1/2 (T202/Y204)
AKT
P-AKT (S473)
mTOR
P-mTOR (S2488)
p70-S6K1
P-p70-S6K1 (T389)
eEF2
P-eEF2 (T56)
CANONICAL HER2 SIGNALING – PROTEIN
G
TOTAL PROTEIN
Protein Content (% of BEN)
p38 MAPK
ERK1/2, 42 kDa
ERK1/2, 44 kDa
Akt
mTOR
p70S6k1
eEF2
H
PHOSPHO/TOTAL PROTEIN
p=0.1
p-p38 MAPK (Y180/Y182)
p-ERK1/2, 42 kDa (T202/T204)
p-ERK1/2, 44 kDa (T202/T204)
p-Akt (S473)
p-mTOR (S2448)
p-p70S6k1 (T389)
p-eEF2 (T56)

Figure 2

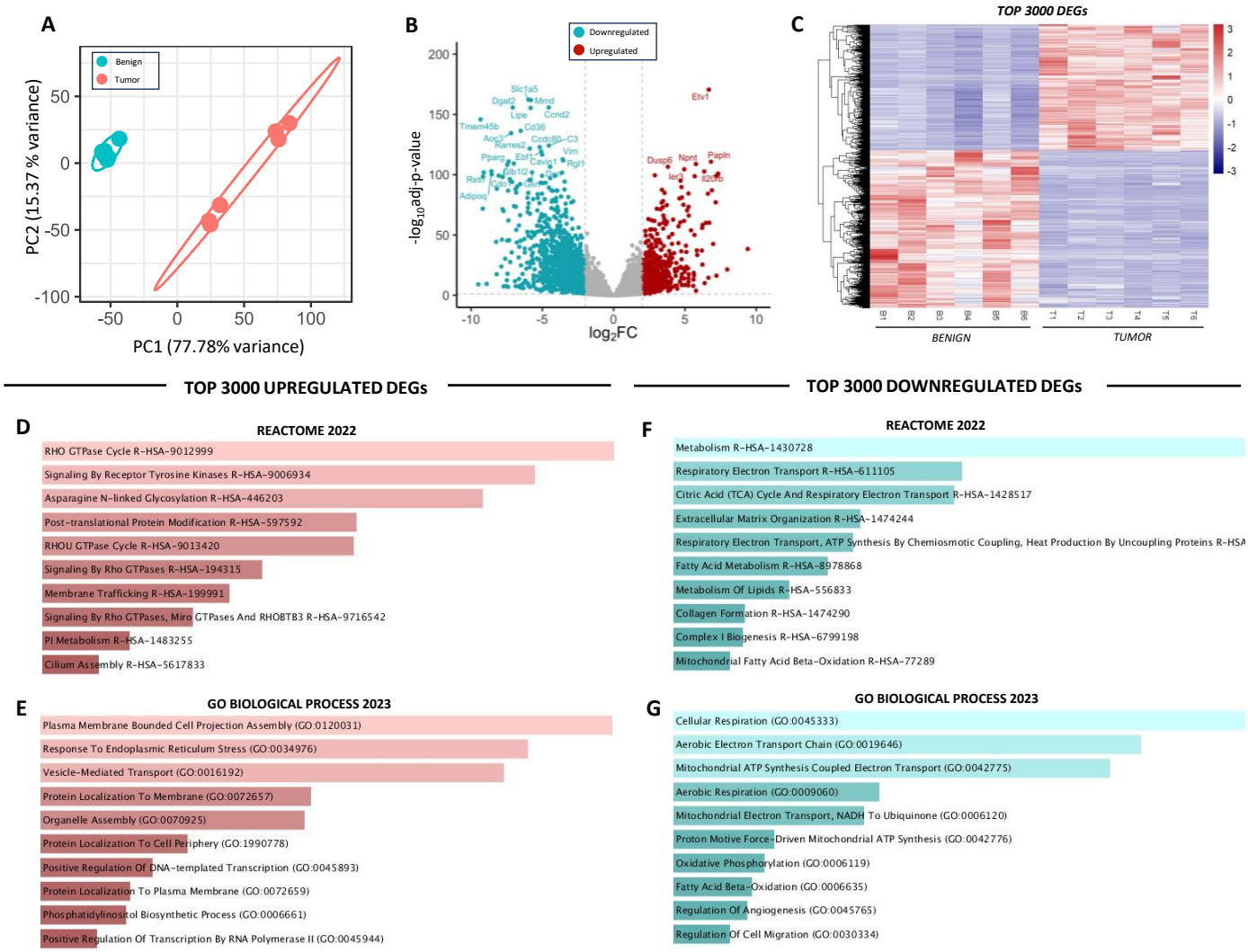
A
Benign
Tumor
PC2 (15.37 % variance)
PC1 (77.78% variance)
B
Downregulated
Upregulated
-log10adj-p-value
log2FC
C
TOP 3000 DEGs
BENIGN
TUMOR
TOP 3000 UPREGULATED DEGs
D
REACTOME 2022
RHO GTPase Cycle R-HSA-9012999
Signaling By Receptor Tyrosine Kinases R-HSA-9006934
Asparagine N-linked Glycosylation R-HSA-446203
Post-translational Protein Modification R-HSA-597592
RHOU GTPase Cycle R-HSA-9013420
Signaling By Rho GTPases R-HSA-194315
Membrane Trafficking R-HSA-199991
Signaling By Rho GTPases, Miro GTPases And RHOBTB3 R-HSA-9716542
PI Metabolism R-HSA-1483255
Cilium Assembly R-HSA-5617833
E
GO BIOLOGICAL PROCESS 2023
Plasma Membrane Bounded Cell Projection Assembly (GO:0120031)
Response To Endoplasmic Reticulum Stress (GO:0034976)
Vesicle-Mediated Transport (GO:0016192)
Protein Localization To Membrane (GO:0072657)
Organelle Assembly (GO:0070925)
Protein Localization To Cell Periphery (GO:1990778)
Positive Regulation Of DNA-templated Transcription (GO:0045893)
Protein Localization To Plasma Membrane (GO:0072659)
Phosphatidylinositol Biosynthetic Process (GO:0006661)
Positive Regulation Of Transcription By RNA Polymerase II (GO:0045944)
TOP 3000 DOWNREGULATED DEGs
F
REACTOME 2022
Metabolism R-HSA-1430728
Respiratory Electron Transport R-HSA-611105
Citric Acid (TCA) Cycle And Respiratory Electron Transport R-HSA-1428517
Extracellular Matrix Organization R-HSA-1474244
Respiratory Electron Transport, ATP Synthesis By Chemiosmotic Coupling, Heat Production By Uncoupling Proteins R-HSA
Fatty Acid Metabolism R-HSA-8978868
Metabolism Of Lipids R-HSA-556833
Collagen Formation R-HSA-1474290
Complex I Biogenesis R-HSA-6799198
Mitochondrial Fatty Acid Beta-Oxidation R-HSA-77289
G
GO BIOLOGICAL PROCESS 2023
Cellular Respiration (GO:0045333)
Aerobic Electron Transport Chain (GO:0019646)
Mitochondrial ATP Synthesis Coupled Electron Transport (GO:0042775)
Aerobic Respiration (GO:0009060)
Mitochondrial Electron Transport, NADH To Ubiquinone (GO:0006120)
Proton Motive Force-Driven Mitochondrial ATP Synthesis (GO:0042776)
Oxidative Phosphorylation (GO:0006119)
Fatty Acid Beta-Oxidation (GO:0006635)
Regulation Of Angiogenesis (GO:0045765)
Regulation Of Cell Migration (GO:0030334)

Figure 3

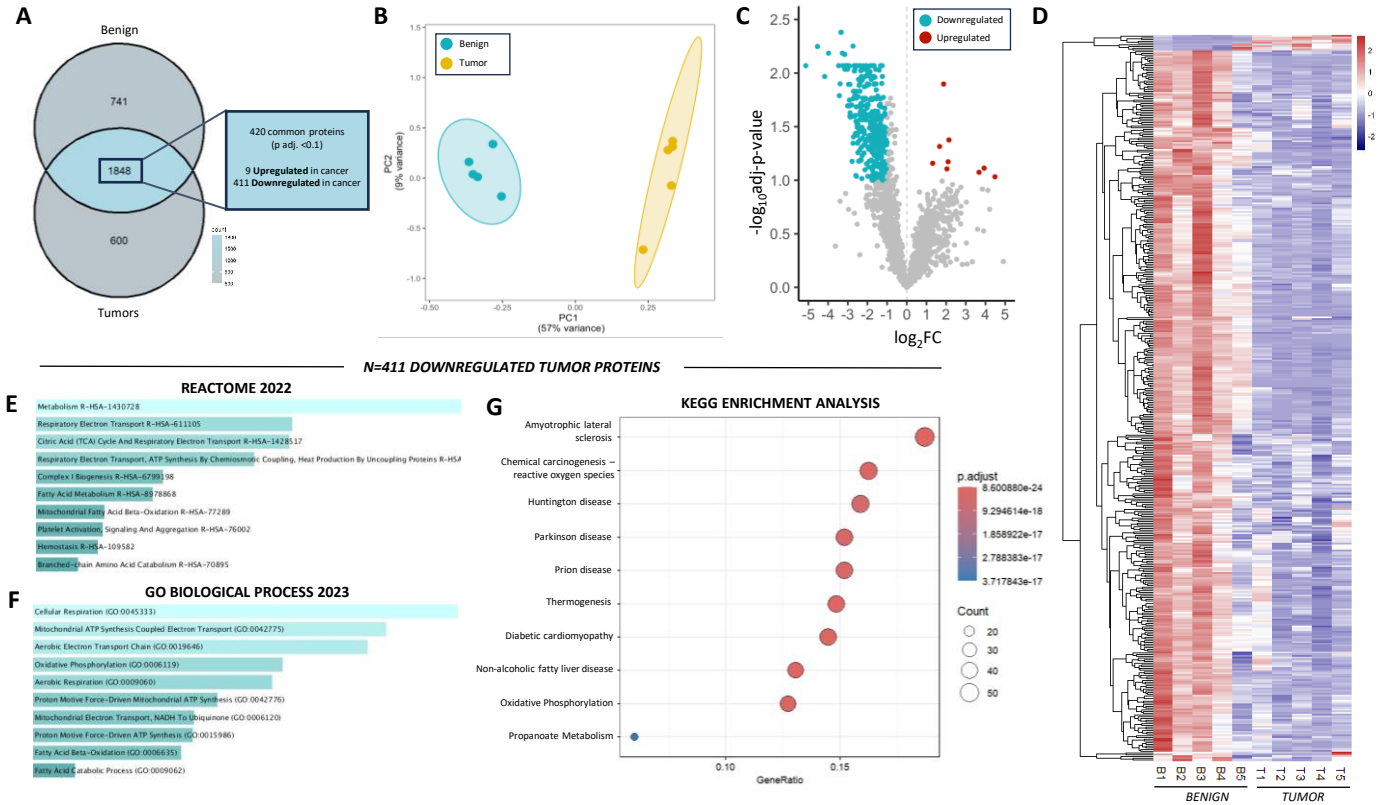
A
Benign
741
1848
600
Tumors
420 common proteins
(p adj. <0.1)
9 Upregulated in cancer
411 Downregulated in cancer
B
Benign
Tumor
PC2
(9% variance)
PC1
(57% variance)
C
Downregulated
Upregulated
-log10adj-p-value
log2FC
D
B1
B2
B3
B4
B5
T1
T2
T3
T4
T5
BENIGN
TUMOR
N=411 DOWNREGULATED TUMOR PROTEINS
E
REACTOME 2022
Metabolism R-HSA-1430728
Respiratory Electron Transport R-HSA-611105
Citric Acid (TCA) Cycle And Respiratory Electron Transport R-HSA-1428517
Respiratory Electron Transport, ATP Synthesis By Chemiosmotic Coupling, Heat Production By Uncoupling Proteins R-HSA
Complex I Biogenesis R-HSA-6799198
Fatty Acid Metabolism R-HSA-8978868
Mitochondrial Fatty Acid Beta-Oxidation R-HSA-77289
Platelet Activation, Signaling And Aggregation R-HSA-76002
Hemostasis R-HSA-109582
Branched-Chain Amino Acid Catabolism R-HSA-70895
F
GO BIOLOGICAL PROCESS 2023
Cellular Respiration (GO:0045333)
Mitochondrial ATP Synthesis Coupled Electron Transport (GO:0042775)
Aerobic Electron Transport Chain (GO:0019646)
Oxidative Phosphorylation (GO:0006119)
Aerobic Respiration (GO:0009060)
Proton Motive Force-Driven Mitochondrial ATP Synthesis (GO:0042776)
Mitochondrial Electron Transport, NADH To Ubiquinone (GO:0006120)
Proton Motive Force-Driven ATP Synthesis (GO:0015986)
Fatty Acid Beta-Oxidation (GO:0006635)
Fatty Acid Catabolic Process (GO:0009062)
G
KEGG ENRICHMENT ANALYSIS
Amyotrophic lateral sclerosis
Chemical carcinogenesis – reactive oxygen species
Huntington disease
Parkinson disease
Prion disease
Thermogenesis
Diabetic cardiomyopathy
Non-alcoholic fatty liver disease
Oxidative Phosphorylation
Propanoate Metabolism
GeneRatio
p.adjust
8.600880e-24
9.294614e-18
1.858922e-17
2.788383e-17
3.717843e-17
Count
20
30
40
50

Figure 4

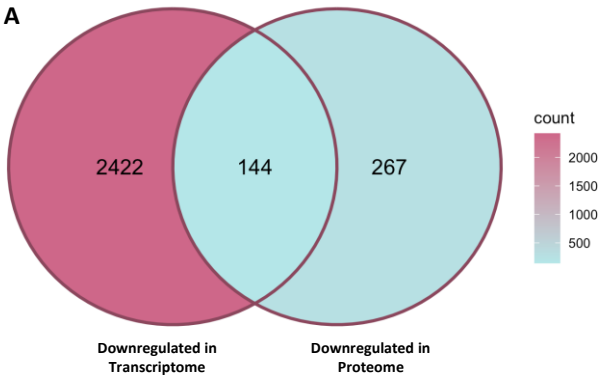
A
2422
144
267
count
2000
1500
1000
500
Downregulated in Transcriptome
Downregulated in Proteome

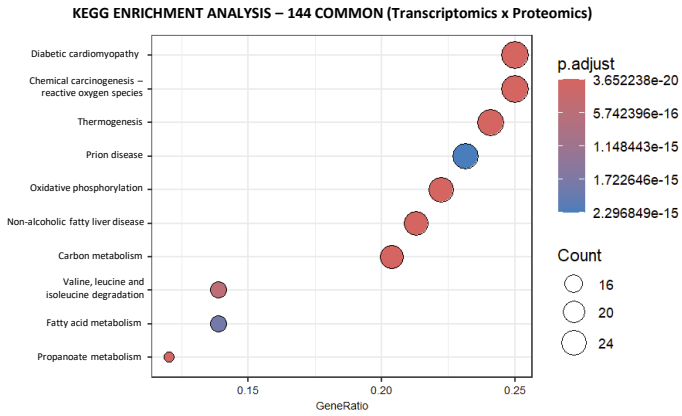
B
KEGG ENRICHMENT ANALYSIS – 144 COMMON (Transcriptomics x Proteomics)
Diabetic cardiomyopathy
Chemical carcinogenesis – reactive oxygen species
Thermogenesis
Prion disease
Oxidative phosphorylation
Non-alcoholic fatty liver disease
Carbon metabolism
Valine, leucine and isoleucine degradation
Fatty acid metabolism
Propanoate metabolism
0.15
0.20
0.25
GeneRatio
p.adjust
3.652238e-20
5.742396e-16
1.148443e-15
1.722646e-15
2.296849e-15
Count
16
20
24

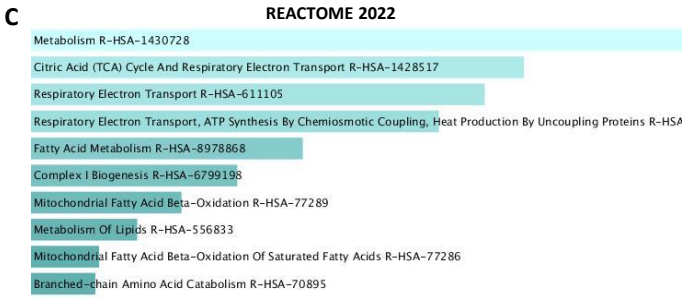
C
REACTOME 2022
Metabolism R-HSA-1430728
Citric Acid (TCA) Cycle And Respiratory Electron Transport R-HSA-1428517
Respiratory Electron Transport R-HSA-611105
Respiratory Electron Transport, ATP Synthesis By Chemiosmotic Coupling, Heat Production By Uncoupling Proteins R-HSA
Fatty Acid Metabolism R-HSA-8978868
Complex I Biogenesis R-HSA-6799198
Mitochondrial Fatty Acid Beta-Oxidation R-HSA-77289
Metabolism Of Lipids R-HSA-556833
Mitochondrial Fatty Acid Beta-Oxidation Of Saturated Fatty Acids R-HSA-77286
Branched-chain Amino Acid Catabolism R-HSA-70895

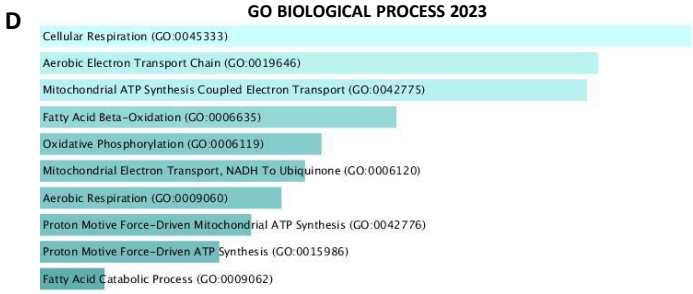
D
GO BIOLOGICAL PROCESS 2023
Cellular Respiration (GO:0045333)
Aerobic Electron Transport Chain (GO:0019646)
Mitochondrial ATP Synthesis Coupled Electron Transport (GO:0042775)
Fatty Acid Beta-Oxidation (GO:0006635)
Oxidative Phosphorylation (GO:0006119)
Mitochondrial Electron Transport, NADH To Ubiquinone (GO:0006120)
Aerobic Respiration (GO:0009060)
Proton Motive Force-Driven Mitochondrial ATP Synthesis (GO:0042776)
Proton Motive Force-Driven ATP Synthesis (GO:0015986)
Fatty Acid Catabolic Process (GO:0009062)

Figure 5

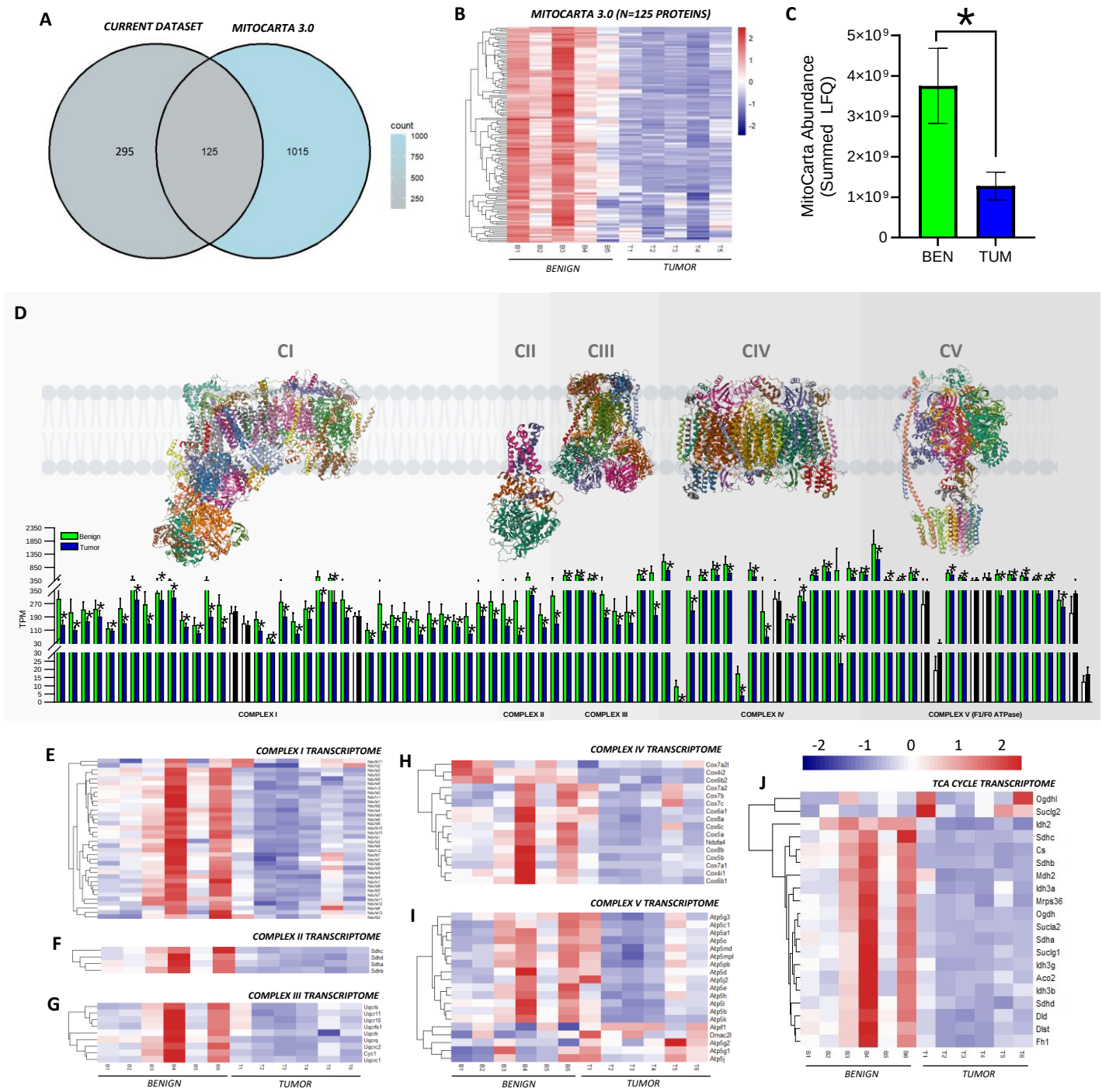
A
CURRENT DATASET
MITOCARTA 3.0
295
125
1015
count
1000
750
500
250
B
MITOCARTA 3.0 (N=125 PROTEINS)
BENIGN
TUMOR
C
MitoCarta Abundance (Summed LFQ)
5×10⁹
4×10⁹
3×10⁹
2×10⁹
1×10⁹
0
BEN
TUM
D
CI
CII
CIII
CIV
CV
Benign
Tumor
TPM
COMPLEX I
COMPLEX II
COMPLEX III
COMPLEX IV
COMPLEX V (F1/F0 ATPase)
E
COMPLEX I TRANSCRIPTOME
F
COMPLEX II TRANSCRIPTOME
G
COMPLEX III TRANSCRIPTOME
H
COMPLEX IV TRANSCRIPTOME
I
COMPLEX V TRANSCRIPTOME
J
TCA CYCLE TRANSCRIPTOME
Ogdhl
Suclg2
Idh2
Sdhc
Cs
Sdhb
Mdh2
Idh3a
Mrps36
Ogdh
Sucla2
Sdha
Suclg1
Idh3g
Aco2
Idh3b
Sdhd
Dld
Dlst
Fh1
BENIGN
TUMOR

Figure 6

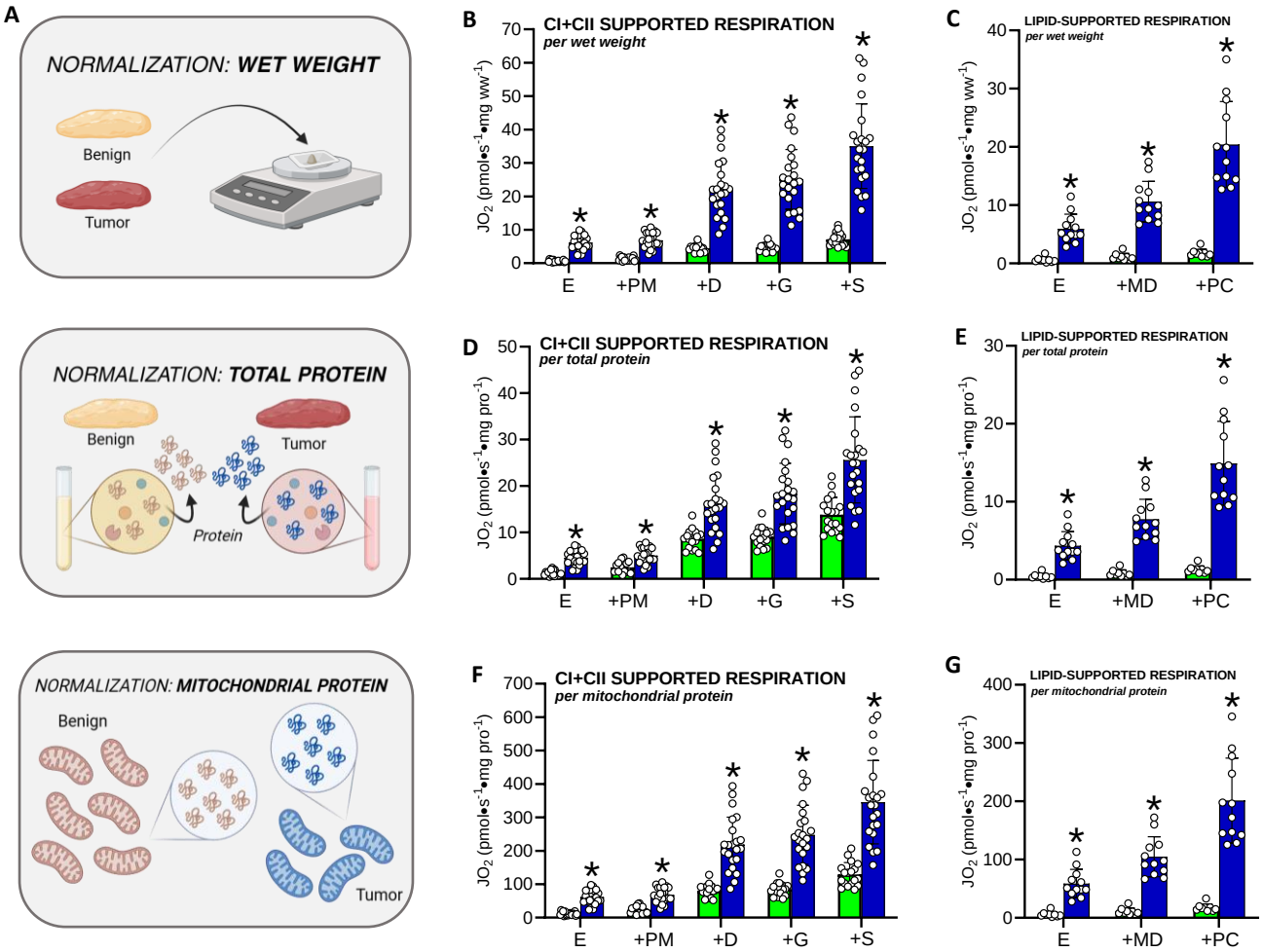
A
NORMALIZATION: WET WEIGHT
Benign
Tumor
NORMALIZATION: TOTAL PROTEIN
Benign
Tumor
Protein
NORMALIZATION: MITOCHONDRIAL PROTEIN
Benign
Tumor
B
CI+CII SUPPORTED RESPIRATION
per wet weight
JO2 (pmol•s-1•mg ww-1)
E
+PM
+D
+G
+S
C
LIPID-SUPPORTED RESPIRATION
per wet weight
JO2 (pmol•s-1•mg ww-1)
E
+MD
+PC
D
CI+CII SUPPORTED RESPIRATION
per total protein
JO2 (pmol•s-1•mg pro-1)
E
+PM
+D
+G
+S
E
LIPID-SUPPORTED RESPIRATION
per total protein
JO2 (pmol•s-1•mg pro-1)
E
+MD
+PC
F
CI+CII SUPPORTED RESPIRATION
per mitochondrial protein
JO2 (pmol•s-1•mg pro-1)
E
+PM
+D
+G
+S
G
LIPID-SUPPORTED RESPIRATION
per mitochondrial protein
JO2 (pmol•s-1•mg pro-1)
E
+MD
+PC

Figure 7

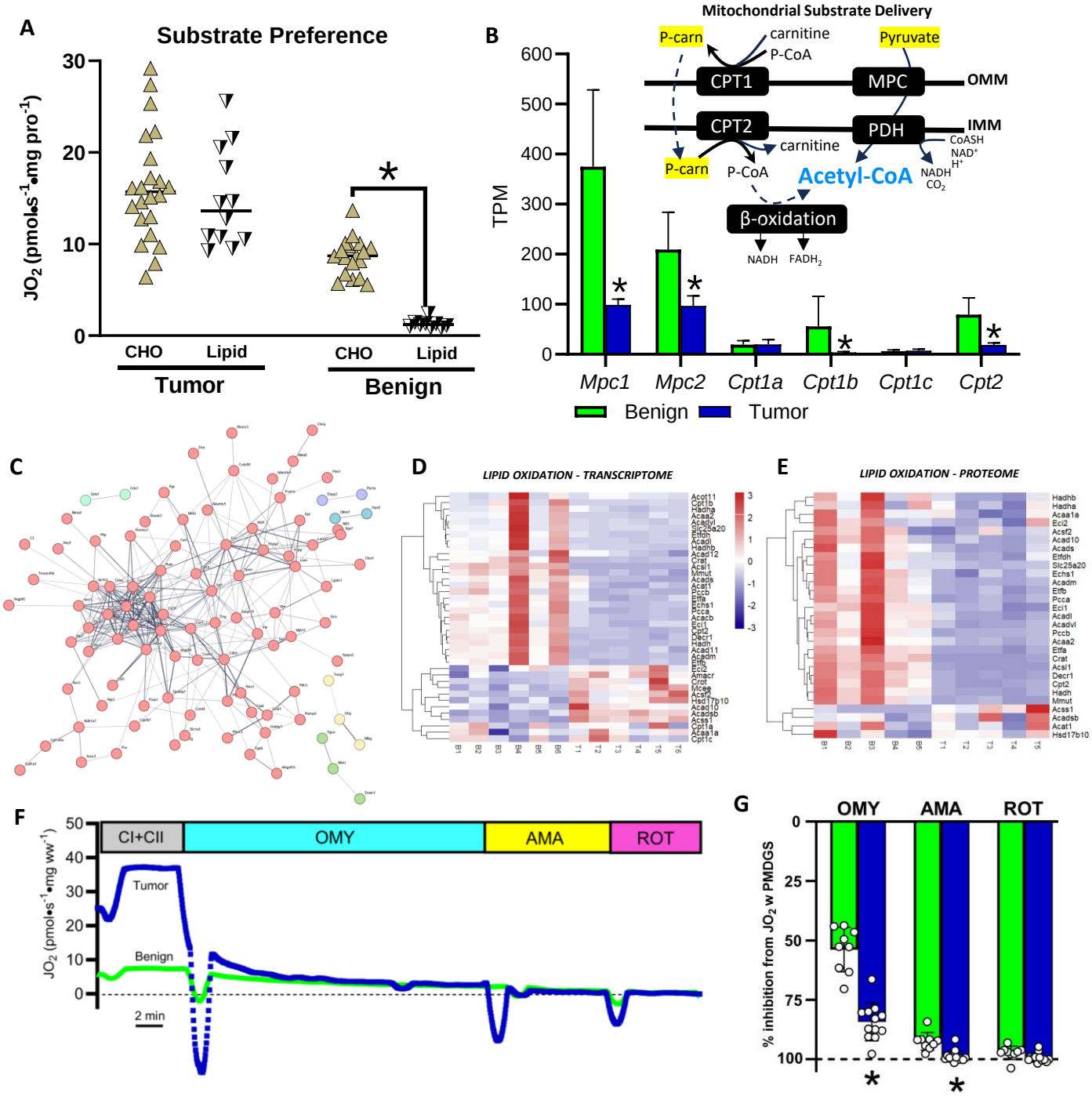
A
Substrate Preference
JO2 (pmol•s-1•mg pro-1)
30
20
10
0
*
CHO
Lipid
CHO
Lipid
Tumor
Benign
B
Mitochondrial Substrate Delivery
P-carn
carnitine
P-CoA
Pyruvate
CPT1
MPC
OMM
CPT2
PDH
IMM
carnitine
P-carn
P-CoA
Acetyl-CoA
CoASH
NAD+
H+
NADH
CO2
β-oxidation
NADH
FADH2
TPM
600
500
400
300
200
100
0
Mpc1
Mpc2
Cpt1a
Cpt1b
Cpt1c
Cpt2
Benign
Tumor
C
D
LIPID OXIDATION - TRANSCRIPTOME
E
LIPID OXIDATION - PROTEOME
F
CI+CII
OMY
AMA
ROT
JO2 (pmol•s-1•mg ww-1)
50
40
30
20
10
0
Tumor
Benign
2 min
G
OMY
AMA
ROT
% inhibition from JO2 w PMDGS
0
25
50
75
100
*
*

Figure 8

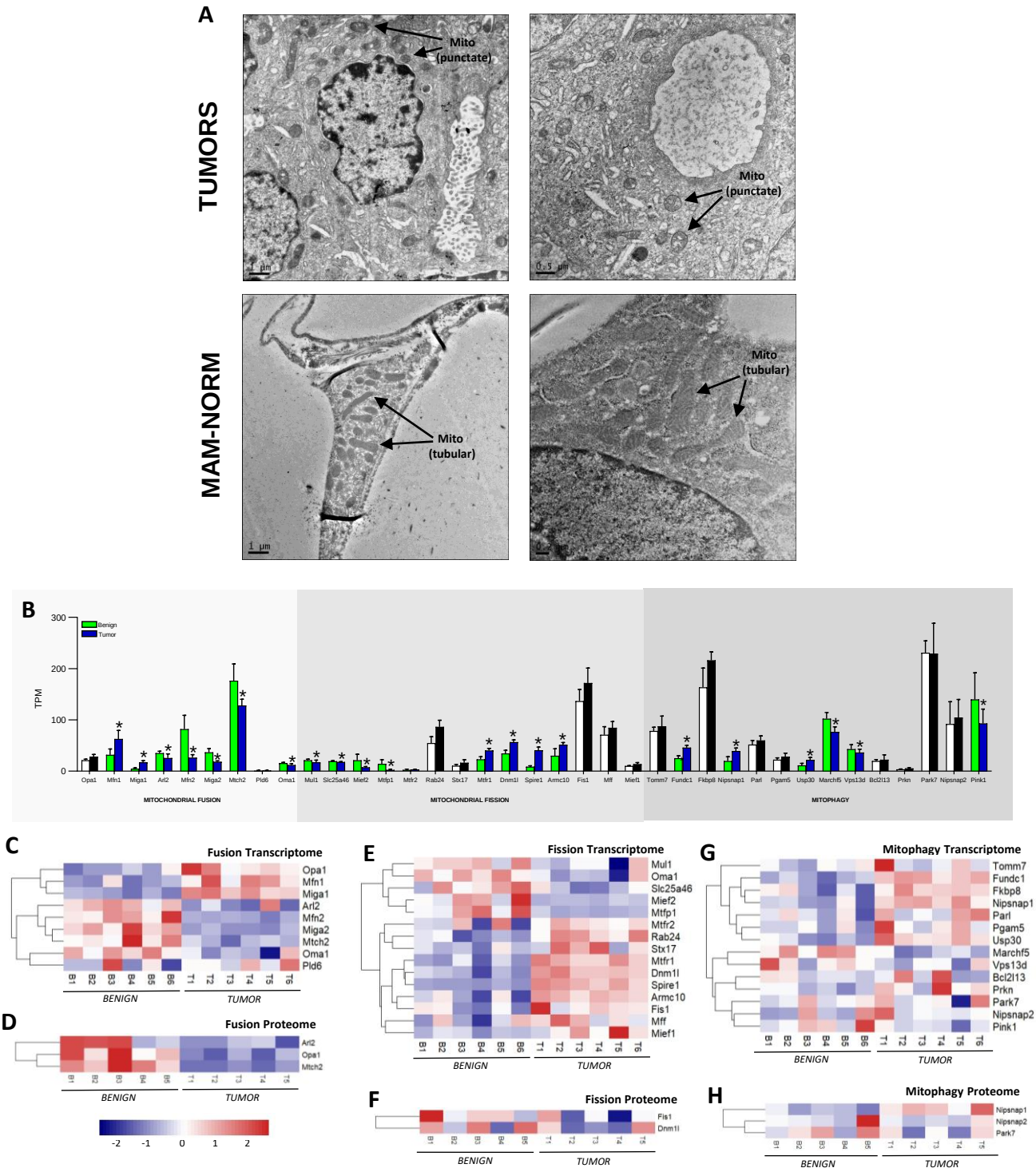
A
TUMORS
MAM-NORM
Mito (punctate)
Mito (punctate)
Mito (tubular)
Mito (tubular)
1 µm
0.5 µm
B
Benign
Tumor
TPM
300
200
100
0
Opa1 Mfn1 Miga1 Arl2 Mfn2 Miga2 Mtch2 Pld6 Oma1 Mul1 Slc25a46 Mief2 Mtfp1 Mtfr2 Rab24 Stx17 Mtfr1 Dnm1l Spire1 Armc10 Fis1 Mff Mief1 Tomm7 Fundc1 Fkbp8 Nipsnap1 Parl Pgam5 Usp30 Marchf5 Vps13d Bcl2l13 Prkn Park7 Nipsnap2 Pink1
MITOCHONDRIAL FUSION
MITOCHONDRIAL FISSION
MITOPHAGY
C
Fusion Transcriptome
Opa1
Mfn1
Miga1
Arl2
Mfn2
Miga2
Mtch2
Oma1
Pld6
B1 B2 B3 B4 B5 B6 T1 T2 T3 T4 T5 T6
BENIGN
TUMOR
D
Fusion Proteome
Arl2
Opa1
Mtch2
BENIGN
TUMOR
-2 -1 0 1 2
E
Fission Transcriptome
Mul1
Oma1
Slc25a46
Mief2
Mtfp1
Mtfr2
Rab24
Stx17
Mtfr1
Dnm1l
Spire1
Armc10
Fis1
Mff
Mief1
BENIGN
TUMOR
F
Fission Proteome
Fis1
Dnm1l
BENIGN
TUMOR
G
Mitophagy Transcriptome
Tomm7
Fundc1
Fkbp8
Nipsnap1
Parl
Pgam5
Usp30
Marchf5
Vps13d
Bcl2l13
Prkn
Park7
Nipsnap2
Pink1
BENIGN
TUMOR
H
Mitophagy Proteome
Nipsnap1
Nipsnap2
Park7
BENIGN
TUMOR

Supplementary Figure 1

CANONICAL HER2 SIGNALING - PROTEIN

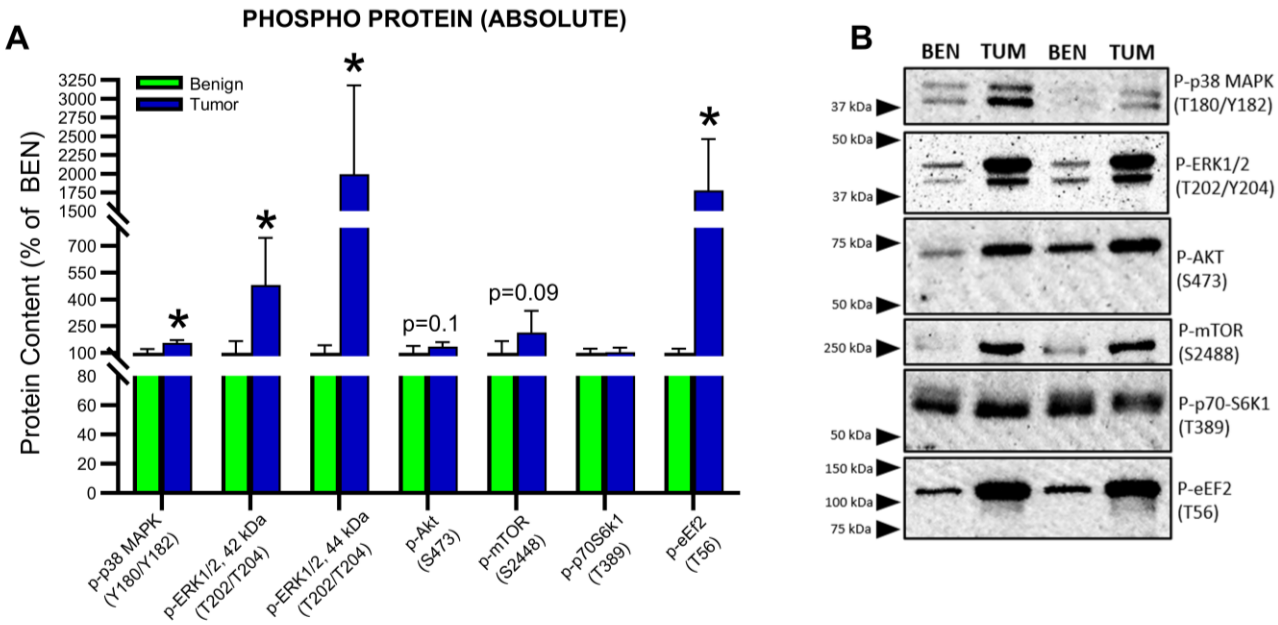

Supplementary Figure 2

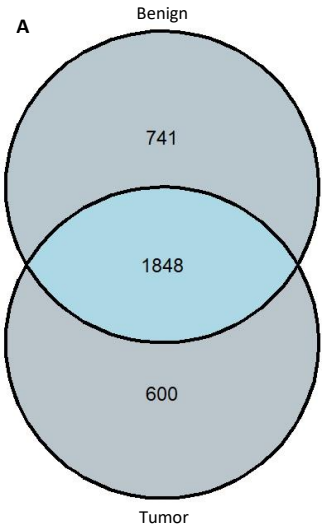

N=741 UNIQUE BENIGN MAMMARY TISSUE PROTEINS

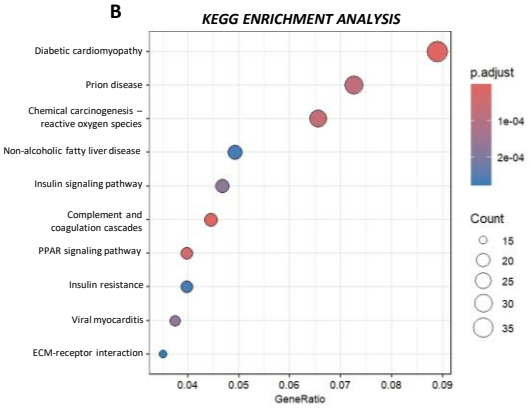

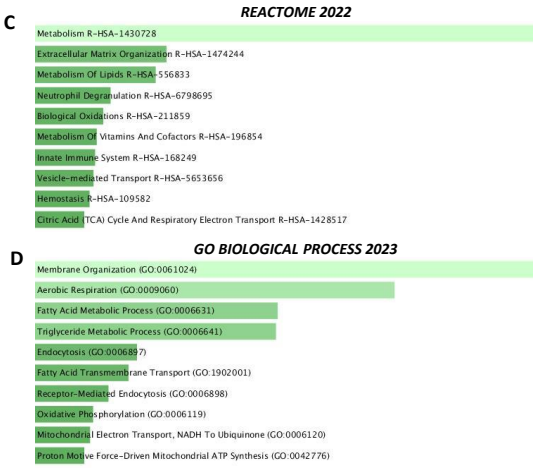

..

N=600 UNIQUE HER2-DRIVEN TUMOR PROTEINS

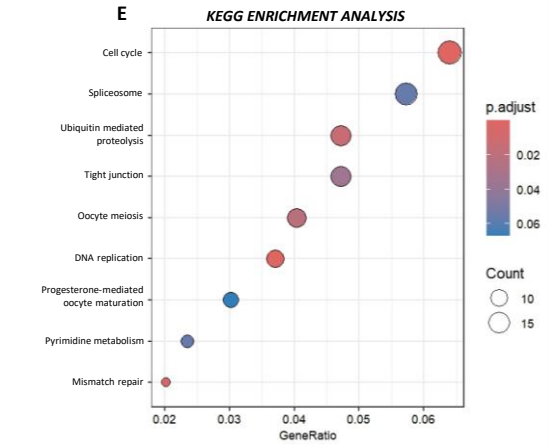

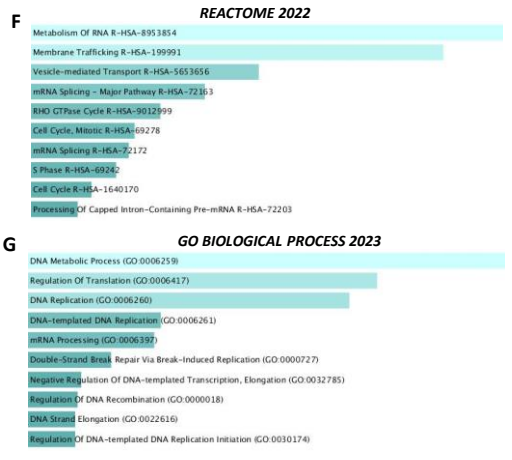

Supplementary Figure 3

$$MEF = \frac{MitoCarta\ Protein\ Abundance}{Total\ Protein\ Abundance}$$

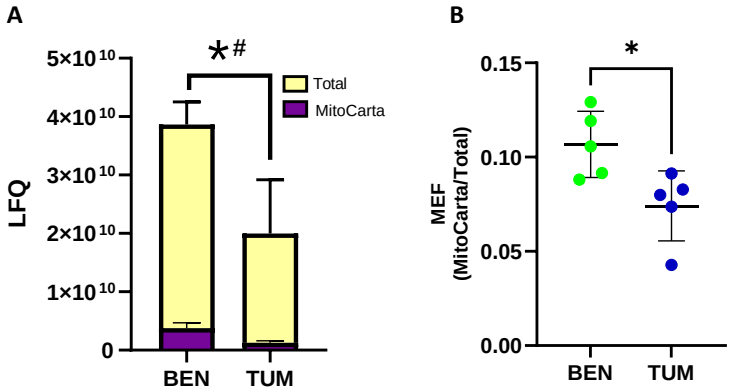

Supplementary Figure 4

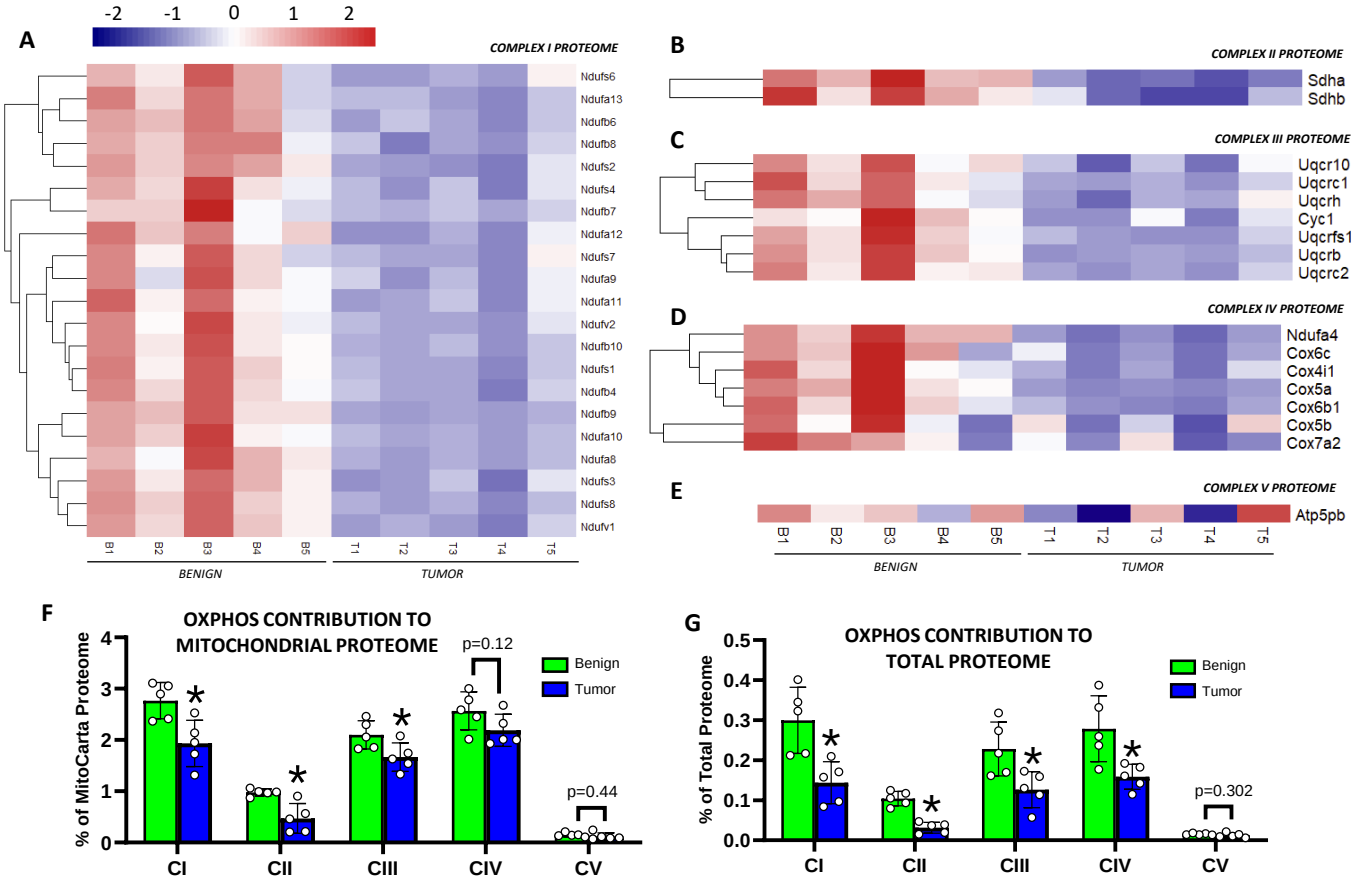

Supplementary Figure 5

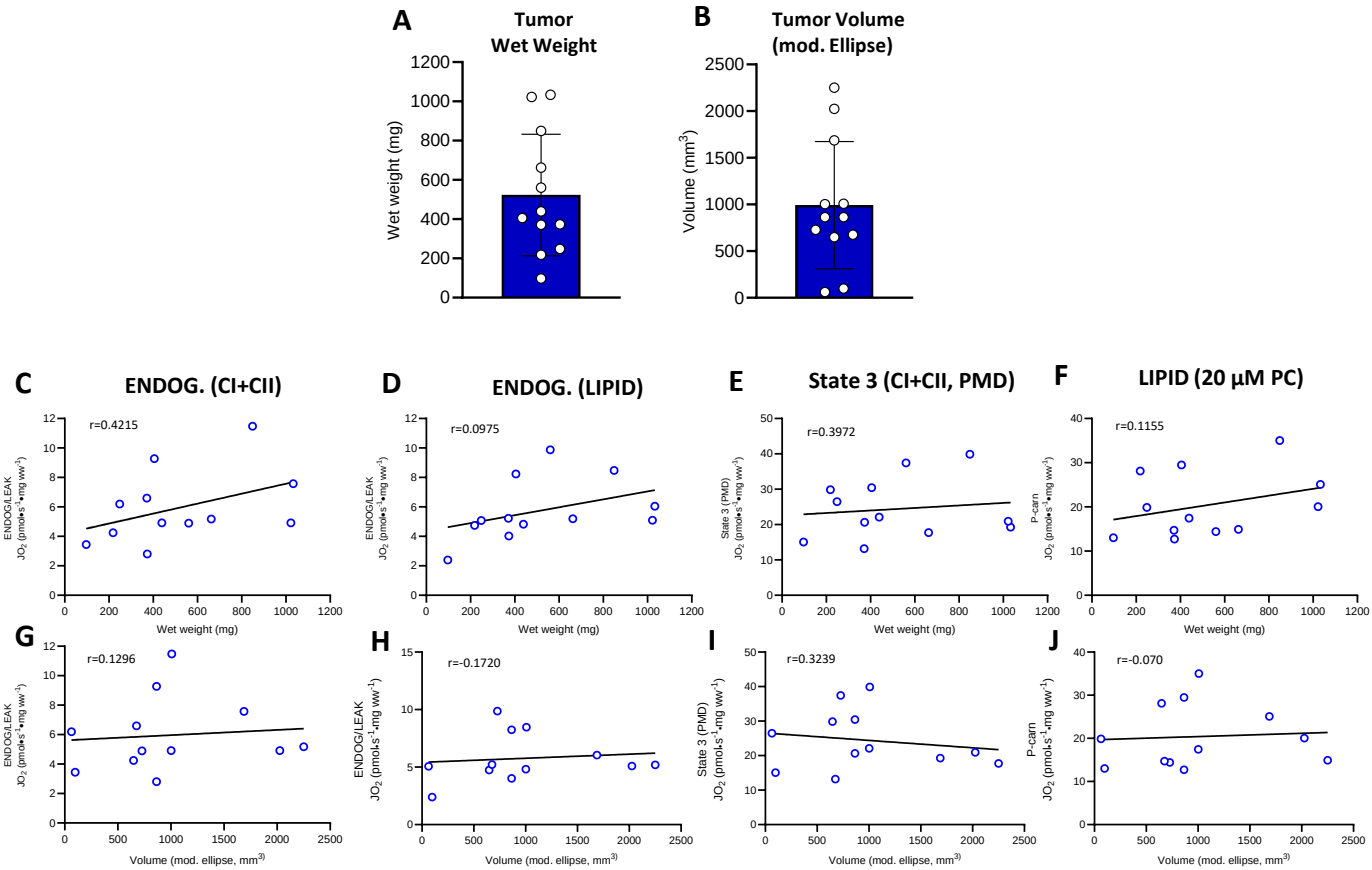

Supplementary Figure 6

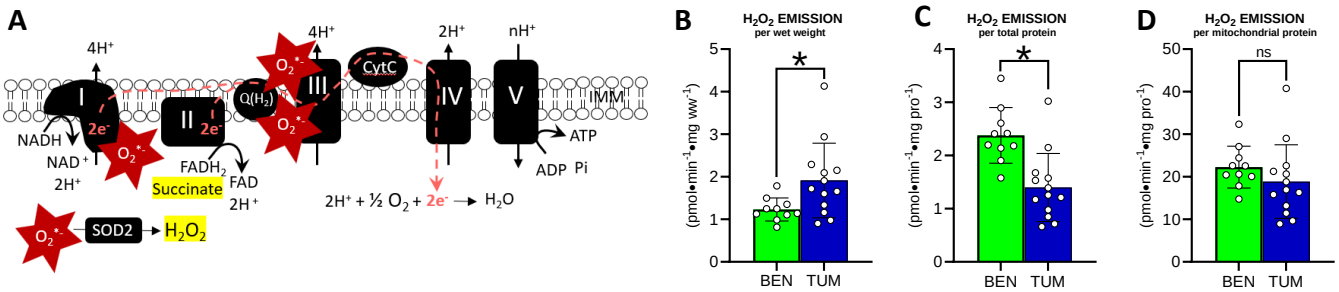

Supplementary Table 1

Abbrev.	Protein	Pathway/Function	Fc (vs BEN)	p.adj
PGK1	Phosphoglycerate kinase	Glycolysis	2.48	0.068
KPYM	Pyruvate kinase	Glycolysis	3.17	0.048
MP2K4	Mitogen activated protein kinase kinase 4	MAPK Pathway	3.65	0.012
RL38	Large ribosomal subunit protein eL38	Protein synthesis/translation	4.11	0.078
PGTA	Geranylgeranyl transferase type-2 subunit alpha	Cysteine prenylation of Rab proteins	4.28	0.067
Rl23	Large ribosomal subunit protein uL14	Protein synthesis/translation	4.41	0.042
CADH1	Cadherin-1	Cell adhesion and motility, epithelial cell marker	12.75	0.084
LMCD1	LIM and cysteine rich domains protein 1	Transcriptional cofactor for GATA6 involved in cell proliferation and metastasis (MMP, EGFR)	15.26	0.077
MPRI	Cation independent mannose 6 phosphate receptor	Lysosomal/Golgi trafficking, associates with IGFR2	22.3	0.093